Reliability of Raman analyses of CO₂-dominated fluid inclusions as a geobarometer at Kīlauea

Charlotte L. Devitre[1], Penny E. Wieser[1]

[1] University of California, Berkeley, Berkeley, CA 94270

We hope that this will inspire new work using FI barometry! We welcome constructive feedback, please reach out to cl.devitre@gmail.com. If our stretching tool is not working for you, please reach out or raise and issue on Github (https://github.com/cljdevitre/RelaxiFI/issues)!

Reliability of Raman analyses of CO₂-dominated fluid inclusions as a geobarometer at Kīlauea

5 Charlotte L. Devitre*[1], Penny E. Wieser[1]
[1] University of California, Berkeley, Berkeley, CA 94270
* cl.devitre@gmail.com [corresponding author]
   ORCiD (FA): 0000-0002-7167-7997

Abstract

Interpreting signals of volcanic unrest requires knowledge of the architecture of the magmatic system,
15 particularly the depths at which magmas are stored. Such information can also be vital to help predict changes in eruptive style and vigour. However, popular petrological tools to assess magma storage depths (e.g., melt inclusions) are costly, present large uncertainties, and are too slow for real-time monitoring. Here, we evaluate the reliability and efficiency of Raman Spectroscopy measurements of CO_2-dominated fluid inclusions as a geobarometer relative to more established methods such as microthermometry and melt inclusion barometry. We
20 calculate storage pressures for 102 olivine-hosted fluid inclusions from the 2018 Lower East Rift Zone eruption of Kīlauea, which are statistically indistinguishable to those determined from melt inclusions. We show that calibrated Raman spectroscopy yields densities within 5-10% of microthermometry measurements for CO_2-dominated fluid inclusions (< 10% mol H_2O in the fluid phase) but is a far more suitable method for systems like Kīlauea dominated by shallow magma storage. Overall, pressures determined from fluid inclusions by Raman spectroscopy are robust,
25 and require only a fraction of the work, time, and resources of melt inclusion studies.

1

Introduction

Determining the depths of magma storage is essential to interpreting signals of volcanic unrest and to help predict changes in eruptive style and vigour. Magma storage depth is commonly determined using erupted materials and petrological tools like melt inclusion, mineral-mineral and mineral-melt barometry (Klügel *et al.*, 2005; Putirka, 2008; Barker *et al.*, 2021). However, many petrological tools present large uncertainties (i.e., ±8-19 km clinopyroxene-based barometers, Wieser *et al.*, 2023), and require extensive sample preparation efforts that make them unsuitable for real-time monitoring. For example, melt inclusion work involves numerous time- and resource-consuming sample preparation, analytical, and data processing steps (Fig. 1). Even after such meticulous work, calculated pressures are typically associated with considerable analytical and systematic uncertainties (e.g., melt and bubble volume measurements, solubility models, post-entrapment crystallization corrections). Such uncertainties can range from 20% to 50% when fully propagated (Tucker *et al.*, 2019; Wieser *et al.*, 2021; DeVitre *et al.*, 2023).

CO_2-dominated fluid inclusions, tiny droplets of exsolved fluids trapped in crystals as they grow in a degassing melt (Roedder, 1979), provide an intriguing alternative to melt inclusions when the main goal is to deduce magma storage depths. The density of CO_2 in an exsolved fluid phase in a melt is a strong function of pressure, with little sensitivity to temperature (Dayton *et al.*, 2023). Thus, if the density of CO_2 captured in a fluid inclusion is well-constrained, and a reasonable estimate is made of entrapment temperature, the entrapment pressure can be directly calculated through an equation of state (Fig. 1). Conventionally, the density of CO_2 in fluid inclusions has been determined by microthermometry through observation of phase changes during heating and cooling – this method has been successfully applied to CO_2-dominated volcanic systems (< 10 mol % H_2O) characterized by deep magma storage systems such as the Canary Islands, Cabo Verde Islands, and the Azores (Klügel *et al.*, 2005, 2020; Zanon and Frezzotti, 2013). However, it is difficult to measure fluid inclusions trapped in shallower volcanic systems (< ~6 km) by microthermometry, because the density of CO_2 is below critical, and the homogenization of the liquid into the vapor phase is nearly impossible to observe optically (Hansteen and Klügel, 2008). Microthermometry also requires the use of specialized heating/cooling stages and the preparation of doubly polished crystal wafers (Fig. 1). The past decade of advances in the accuracy and precision of Raman-based CO_2 densimetry has opened new avenues for the technique (Lamadrid *et al.*, 2017; DeVitre *et al.*, 2021). Specifically, Raman can measure the density of very small fluid inclusions (down to ~1 um) and/or those with low bulk CO_2 densities (<0.45 g/cm^3) which are impossible to measure by microthermometry with an accuracy of ~0.02 g/cm^3 (Yuan and Mayanovic, 2017). Raman analyses also only require a single polish to ensure visibility of the

2

fluid inclusions within ~50 μm of the surface, resulting in fewer preparation steps than necessary for both microthermometry and melt inclusion workflows (Fig. 1). Raman also has the advantage of being commonly used in fields like chemistry, biology, material science and physics and therefore instrumentation is available at many research institutions. Recent work also indicates that fluid inclusions may have potential as a real-time petrological monitoring tool as they can be used to relatively rapidly constrain the depth of magma storage (Dayton *et al.*, 2023).

Nevertheless, fluid inclusions are often prone to a variety of post-entrapment modifications, such as stretching and decrepitation and may be subject to significant re-equilibration prior to eruption (e.g., Wanamaker and Evans, 1989; Hansteen and Klügel, 2008). Re-equilibration is often thought to be rapid, such that fluid inclusions may reflect stalling levels rather than true capture depths (Hansteen and Klügel, 2008; Zanon and Frezzotti, 2013), or even be reset during slow quenching (Klügel *et al.*, 2020). This brings us to an essential question as Raman-based fluid inclusion barometry grows in popularity: are the storage depths estimated using CO_2-dominated fluid inclusions consistent with those constrained by melt inclusion barometry and other estimates of magma storage depths or are they always reset by late-stage processes as magmas ascend to the surface?

The 2018 Lower East Rift Zone (LERZ) eruption of Kīlauea volcano in Hawai'i is an ideal test bed to assess fluid inclusion barometry, given that this volcano is extremely well monitored, and geophysical methods have revealed two main regions of magma storage (1-2 km depth, and ~3-5 km, Baker and Amelung, 2012; Anderson and Poland, 2016; Anderson *et al.*, 2019). These geophysical estimates were corroborated by melt inclusion work on erupted 2018 samples (Lerner *et al.*, 2021; Wieser *et al.*, 2021). However, it is notable that both melt inclusion studies were submitted ~2 years after the eruption had ended, a testament of the considerable analytical effort required (Fig. 1), and thus the unsuitability of this method as a monitoring tool. Here, we assess whether magma storage depths determined using Raman analyses of CO_2-dominated fluid inclusions would have yielded the same results. First, we evaluate the accuracy of the Raman method through a direct comparison with microthermometry to validate our approach to determine entrapment pressures. Then, we compare pressures from 102 fluid inclusions hosted in olivine crystals to those of melt inclusion from the exact same samples (and sometimes even the same crystals). Our results show that magma storage depths calculated from fluid inclusion barometry and melt inclusion barometry are statistically indistinguishable, yet fluid inclusions have significantly smaller uncertainties, and require far fewer preparation and analytical steps (Fig. 1).

3
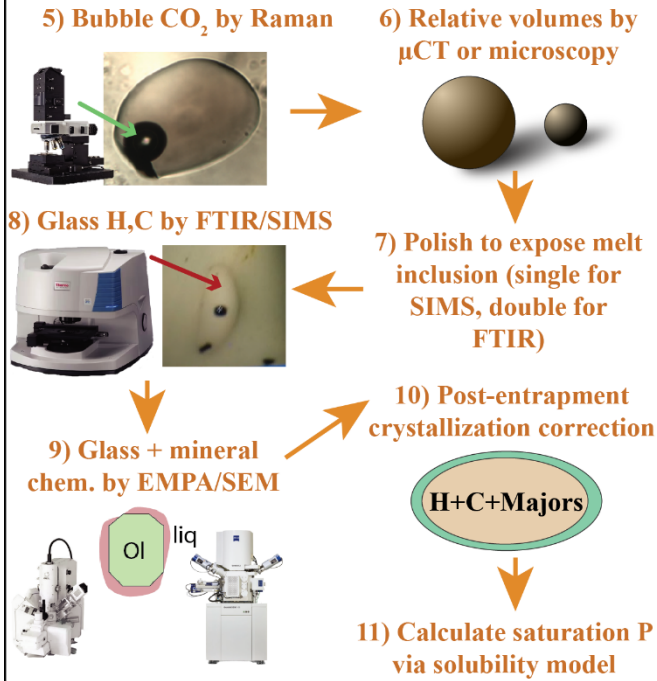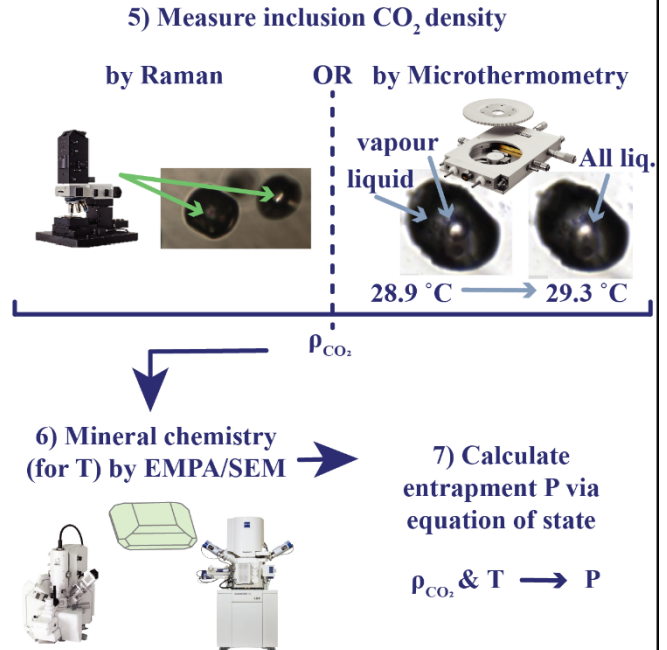
Figure 1: melt inclusion and fluid inclusion workflows for magma storage depths measurements. Melt inclusion workflow steps are in orange-coloured text and fluid inclusion steps are in blue.

## Calibrated Raman spectroscopy is a suitable alternative to microthermometry

Despite its relative ease compared with microthermometry, and ability to assess a wider range of CO_2 densities, many aspects of the Raman method have been recently criticized (e.g., peak fitting, instrument drift, instrument calibrations), with suggestions it is '150X less accurate than microthermometry' (Bakker, 2021). To

4

assess whether Raman spectroscopy can reliably be used to measure the density of CO_2-dominated fluid inclusions,

95   we measured olivine-hosted fluid inclusions from Fogo volcano, Cabo Verde (DeVitre *et al.*, 2023) using both our calibrated Raman instrument and microthermometry (ρ_{CO2} > ~0.45 g/cm³; Fig. 2a ; Fig. S-4 in SI Appendix). We measured the inclusions on the Raman while maintaining a constant temperature of 37 ˚C and at low-laser power to mitigate potential effects of laser-induced heating on measured fermi diad separation (Hagiwara *et al.*, 2021). Melting temperatures for all fluid inclusions analysed using microthermometry (11 crystals, ~60 fluid inclusions)

100   are -56.5 ± 0.1 ˚C (Fig. 2a) which precludes the significant presence of any gaseous species other than CO_2 (confirmed via Raman Spectroscopy). Homogenization temperatures obtained range from -11.1±0.1 to 31.6±1 ˚C (Fig. S-4b) and yield calculated bulk densities between 0.49 and 0.99 g/cm³ (Fig. 2a). Results of microthermometry and calibrated Raman spectroscopy are generally within 5% of each other (Fig. 2a), and up to 10% for inclusions with near-critical CO_2 densities (~0.45 g/cm³), where microthermometry become extremely sensitive to the

105   accuracy of the homogenization temperature and the phase transition is difficult to constrain (Hansteen and Klügel, 2008). Regression statistics confirms good agreement between the two methods (R^2=0.96, RMSE=0.02 g/cm³, p-val<0.000). Overall, this comparison validates Raman spectroscopy measurements as a suitable alternative to microthermometric measurements (see also Kobayashi *et al.*, 2012).
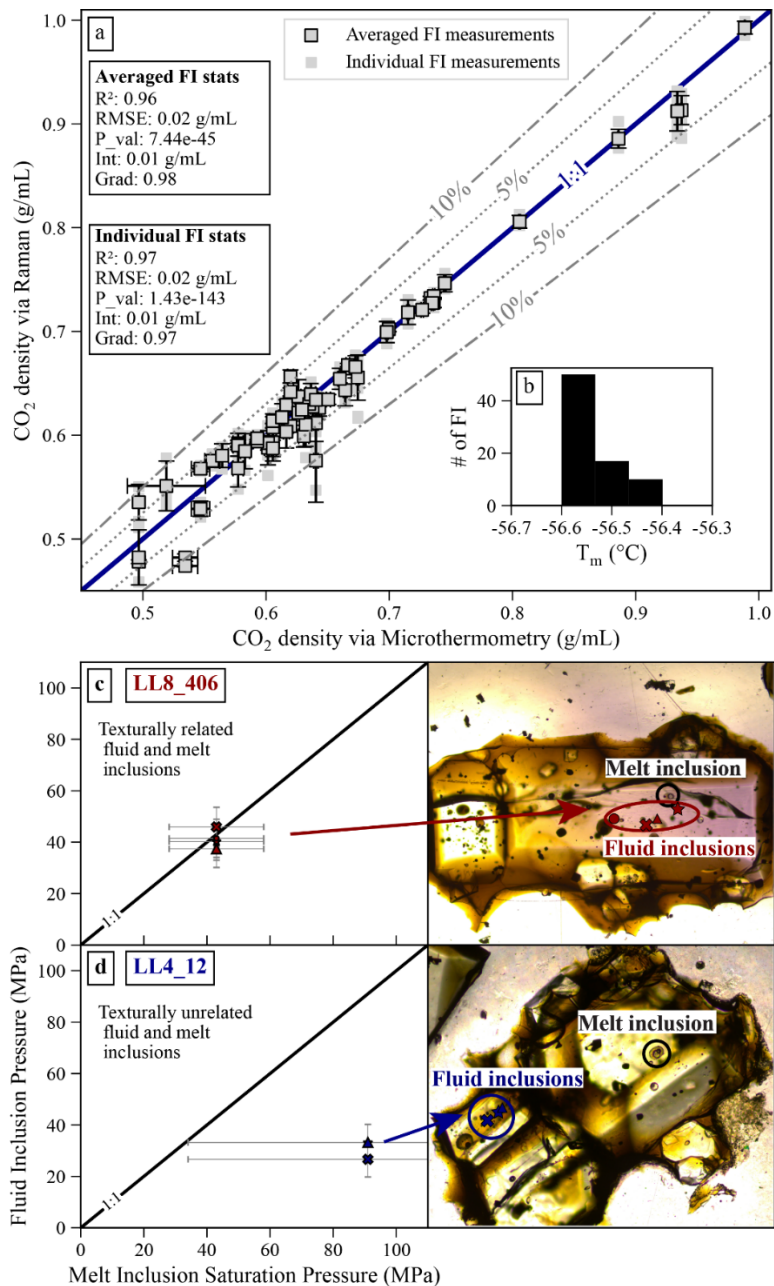
Figure 2: Comparison of Raman spectroscopy vs. Microthermometry, and melt inclusion barometry vs. fluid inclusion barometry. (a) Density via Raman vs density obtained from micro thermometry. Outlined symbols represent averaged Raman measurement for each fluid inclusion, no-outline symbols are individual Raman measurements. Error bars show ±1σ of repeated measurements for Raman and microthermometry. (b) Crystal with clearly texturally related melt inclusions and fluid inclusions (LL8_406) showing overlapping pressures. (c) Crystal with texturally-unrelated melt inclusions and fluid inclusions (LL4_12)– fluid inclusions are found in a smaller olivine crystal in the same crystal cluster and return lower pressures. Specific crystal plots and images for every other pair identified are provided in the SI Image Database for detailed comparisons.

6

fluid and melt inclusion pressures yield a consistent petrogenetic model

Now that we have validated the Raman method to measure CO_2 densities, we wish to test whether fluid inclusion pressures are a suitable alternative to the more widely used melt inclusion method. The most robust comparison examines pressures from melt inclusions and fluid inclusions within a single crystal. Therefore, we analysed 36 CO_2-dominated fluid inclusions in 17 crystals containing melt inclusions measured by Wieser *et al.* (2021, Fig. 2). Petrographic work was done to categorize fluid inclusions depending on their shapes, position, and approximate textural relationship to the melt inclusions. We remove fluid inclusions with a significant melt film (>20% vol) and poor-quality Raman analyses (see SI Appendix). Overall, we find that fluid inclusions hosted in the same crystals, same inclusion assemblages or apparent growth zones record the same entrapment pressures as reconstructed melt inclusions within the uncertainty of the methods (Fig. 2b). In contrast, texturally unrelated fluid inclusions and melt inclusions (e.g., the fluid inclusion is present in the same crystal cluster but within a separate smaller crystal) tend to yield different pressures (Fig. 2d). If crystals were attached via synneusis (Wieser *et al.*, 2019; DiBenedetto *et al.*, 2020), it is very plausible the smaller crystal grew in a different environment, explaining the lower fluid inclusion pressure (Fig. 2e). In general, it appears that if fluid inclusions are well documented and selected with care (i.e., fluid inclusions in crystal core growth zones), the estimates of pressure for fluid inclusions are consistent with those from melt inclusion work at Kīlauea.

The large error on melt inclusions pressures is notable during these comparisons and mainly results from uncertainty in the relative volume of the vapour bubble (Fig.3 orange MI w/VB error bar; Wieser et al., 2021, Tucker 2019, others). The uncertainties on CO_2-dominated fluid inclusion pressures are much smaller as they are only a result of peak-fitting, drift corrections, and uncertainty in the temperature of fluid trapping/re-equilibration (Wieser and DeVitre, 2023). These sources of uncertainty were propagated in DiadFit (Wieser and DeVitre, 2023) using Monte Carlo simulations considering 50 K uncertainty on the temperature (see supporting information for details on temperature) and a 1σ uncertainty on density based on peak-fit uncertainties of CO_2 spectra as well as the uncertainty in the Ne correction model. We also correct pressures for the presence of H_2O in the exsolved fluid using the mixed CO_2-H_2O EOS of Duan and Zhang (2006) using X_{H2O} values inferred from melt inclusion data at Kīlauea (Wieser *et al.*, 2021), further propagating the additional uncertainty introduced by this correction step (see SI Appendix section 3).

Due to the scarcity of fluid inclusions in the exact same crystal as melt inclusions, direct comparisons are limited. To complement our dataset, we also analysed an additional 109 fluid inclusions in olivine crystals picked directly from the same sample split as the melt inclusions. After filtering those with >20% melt film and poor-

quality spectra, we report a total of 102 fluid inclusions and compare them with 103 melt inclusions from Wieser *et al.*, 2021. When subdivided by sample (May, July, Aug 2018), histograms indicate good agreement between the pressures recorded by fluid inclusions and melt inclusions (Fig. 3 a-c), particularly when considering the analytical uncertainty associated with melt inclusions measurements.

We apply the Kolmogorov–Smirnov test (KS) to assess whether slight visual differences are statistically significant. Sample KS tests indicate that melt inclusion and fluid inclusion pressures are not significantly different for May and August 2018 (p-val = 0.16 and 0.03 respectively) but suggest a possible significant difference for July 2018 (p-val=0.001). However, such comparisons are restricted by the relatively small N for each sample (N<50), and the relatively large analytical errors on melt inclusion measurements. To address this, we apply a Monte-Carlo simulation using Python3 to resample each melt inclusion and fluid inclusion measurement 1000 times within analytical uncertainty. KS tests applied to these resampled distributions indicate that the fluid inclusion and melt inclusion pressure distributions are not significantly different for any of the 3 events (p-val = 0.44 ± 0.19, 0.02 ± 0.03 and 0.05 ± 0.05 for May, July and August respectively) and differences can be explained by the uncertainty in the melt inclusion measurements.

So far, we have only considered the analytical uncertainty associated with melt inclusion and fluid inclusion saturation pressures. However, reconstructed melt inclusion H_2O and CO_2 concentrations are converted into pressures using a solubility model, which introduces a large amount of systematic uncertainty (see Wieser *et al.*, 2022). On Fig. 3g-i, we show pressures calculated using the MagmaSat model (Ghiorso and Gualda, 2015), which Wieser *et al.*, 2021 suggest is the most suitably calibrated model at Kīlauea. However, this is little consensus; for the same eruption, Lerner *et al.*, 2021 use the solubility model of Iacono-Marziano *et al.* (2012). Cumulative melt inclusion pressures for 5 different solubility models (Newman and Lowenstern, 2002; Iacono-Marziano *et al.*, 2012; Shishkina *et al.*, 2014; Ghiorso and Gualda, 2015; Allison *et al.*, 2022) clearly show that the uncertainty related to model choice can easily account for any slight differences between melt inclusion and fluid inclusion pressures (Fig. S-9 in SI). Another advantage of fluid inclusion barometry compared to melt inclusion barometry is that the choice of EOS does not significantly contribute to the uncertainty (Hansteen and Klügel, 2008).

Slight differences between fluid inclusion and melt inclusion pressures could also be explained through sampling bias relating to the complex histories of the 2018 crystal cargo. Lerner *et al.*, 2021 and Wieser *et al.*, 2021,suggest that crystals are derived from two storage reservoirs beneath Kilauea's summit based on the relationship between melt inclusion saturation pressures, entrapment depths and olivine Fo content. Specifically, Wieser *et al.*, (2021) report a entrapment depth of 0.89-1.74 km for low-Fo (<81.5 Fo) olivines in equilibrium with the carrier melt and ~ 2-5 km for high-Fo (>81.5 Fo) olivines which correlate well with previously proposed

8

geophysical estimates of depths for the two magma reservoirs at Kīlauea (Poland *et al.*, 2014; Anderson *et al.*,
2019). Fluid inclusion pressures confirm this relationship – those trapped in lower Fo content olivine crystals tend
to have lower pressures of entrapment (Fig. 3g-i). This demonstrates that similar petrogenetic interpretations can
be made with both fluid inclusions and melt inclusions.
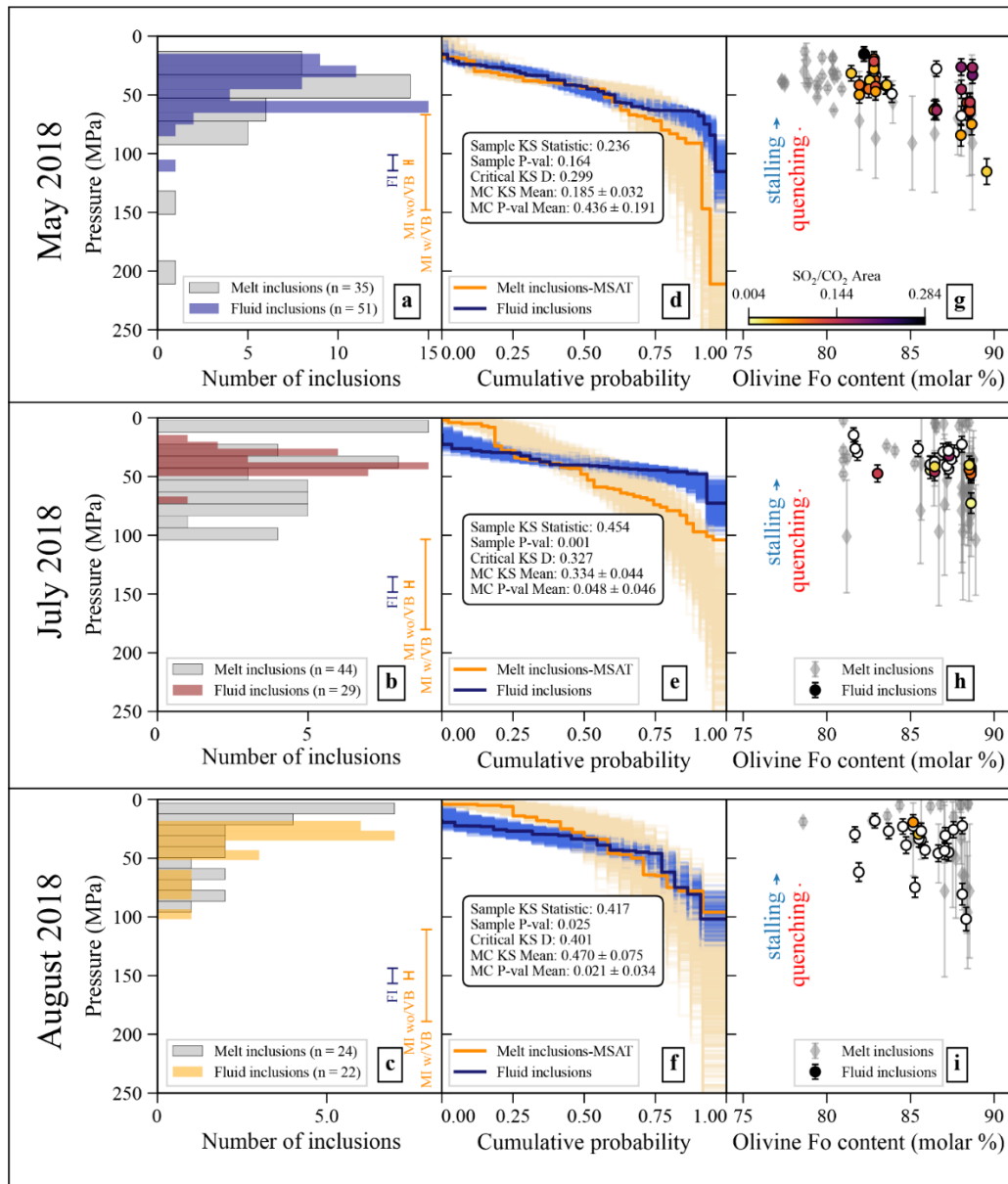
Figure 3: Comparing fluid inclusion and melt inclusion pressures for May, July and August 2018. a-c) Histograms of pressures, with error bars indicate the average 1σ uncertainty for melt inclusions with vapor bubbles (melt inclusion w/VB) and without vapor bubbles (melt inclusion wo/VB), and the average 1σ fluid inclusion uncertainty. (d-f)

190 **Results of KS tests comparing fluid inclusion and melt inclusion pressure cumulative probability functions (CDF) from Monte-Carlo simulations. For melt inclusions, the MagmaSat results are shown (further details and solubility models in supplement, including MagmaSat (MSAT), Shishkina (SHISHKINA), Iacono-Marziano (IM), MafiCH (MAFICH), VolatileCalc (VOLATILECALC) (Newman and Lowenstern, 2002; Iacono-Marziano *et al.*, 2012; Shishkina *et al.*, 2014; Ghiorso and Gualda, 2015; Allison *et al.*, 2022)). (g-i) melt inclusion and fluid inclusion pressures vs Fo content of the host olivine for (g) May 2018 (h) July 2018 (i) August 2018. fluid inclusions are coloured by calculated SO_2 (mol%) based on the method of Burke (2001).Arrows depicting the effect of stalling and quenching on fluid inclusions (modelled in Fig 4).**

Assessing fluid inclusion re-equilibration

195

Although differences between melt inclusions and fluid inclusions are not statistically significant (Fig. 3d-f), some fluid inclusions do appear to record shallower pressures than melt inclusions for an equivalent olivine Fo content (i.e., Fig. 3e and h). Whereas melt inclusions suffer from large systematic uncertainties related to solubility models (Fig. S-9 in SI), the main source of such uncertainty affecting CO_2-dominated fluid inclusions is the process

200 of re-equilibration during prolonged storage and transport. To assess whether re-equilibration could explain the seemingly lower pressures recorded by fluid inclusions in July 2018, we constructed a Python3 implementation of the mechanical re-equilibration model of Wanamaker and Evans (1989) based on olivine relaxation through dislocation creep (RelaxiFI, see Data Availability). We model the effect of fluid inclusion stretching on the internal pressure and CO_2 density for fluid inclusions using the EOS of (Span and Wagner, 1996). We consider fluid

205 inclusions with a radius of 1 and 20 µm at variable distances (50-500 µm) from crystal defect structures (i.e., cracks, crystal edges and boundaries). It has also been suggested that fluid inclusions erupted in lava flows may re-equilibrate as the host crystal cools at atmospheric pressure (Klügel *et al.*, 2020). The May-18 sample is a rapidly quenched reticulite, and the Aug-18 sample was water-quenched from the lava channel. In contrast, the July-18 sample was an air-cooled overflow from the channel. Based on observing the formation and quenching of other

210 overflows, we predict that cooling occurred within hours. However, even allowing up to 7 days re-equilibration results in less than 1% difference (Fig. 4a-b), well within analytical uncertainty. Next, we consider a FI which may have been trapped in the deeper South Caldera reservoir (~4 km, 1300 ˚C) before being mobilized to the Halemaʻumaʻu reservoir (~1 km depth, 1150 ˚C), and stored for 0-2 years prior to eruption (based on diffusion timescales from Mourey *et al.*, 2023, Fig. 4c-d). In the most extreme case (stretching of a 20 µm radius fluid

215 inclusion found 50 µm from a crystal defect), stalling for 2 years causes a decrease in CO_2 density of less than 10%, which is smaller than the average measurement uncertainty.

Overall, our results indicate that in shallow systems such as that of Kīlauea where the internal pressure of the fluid inclusion is relatively low, stretching on timescales relevant to magma storage, eruption and quenching is unlikely to play a major role and re-equilibration is of no significant concern.
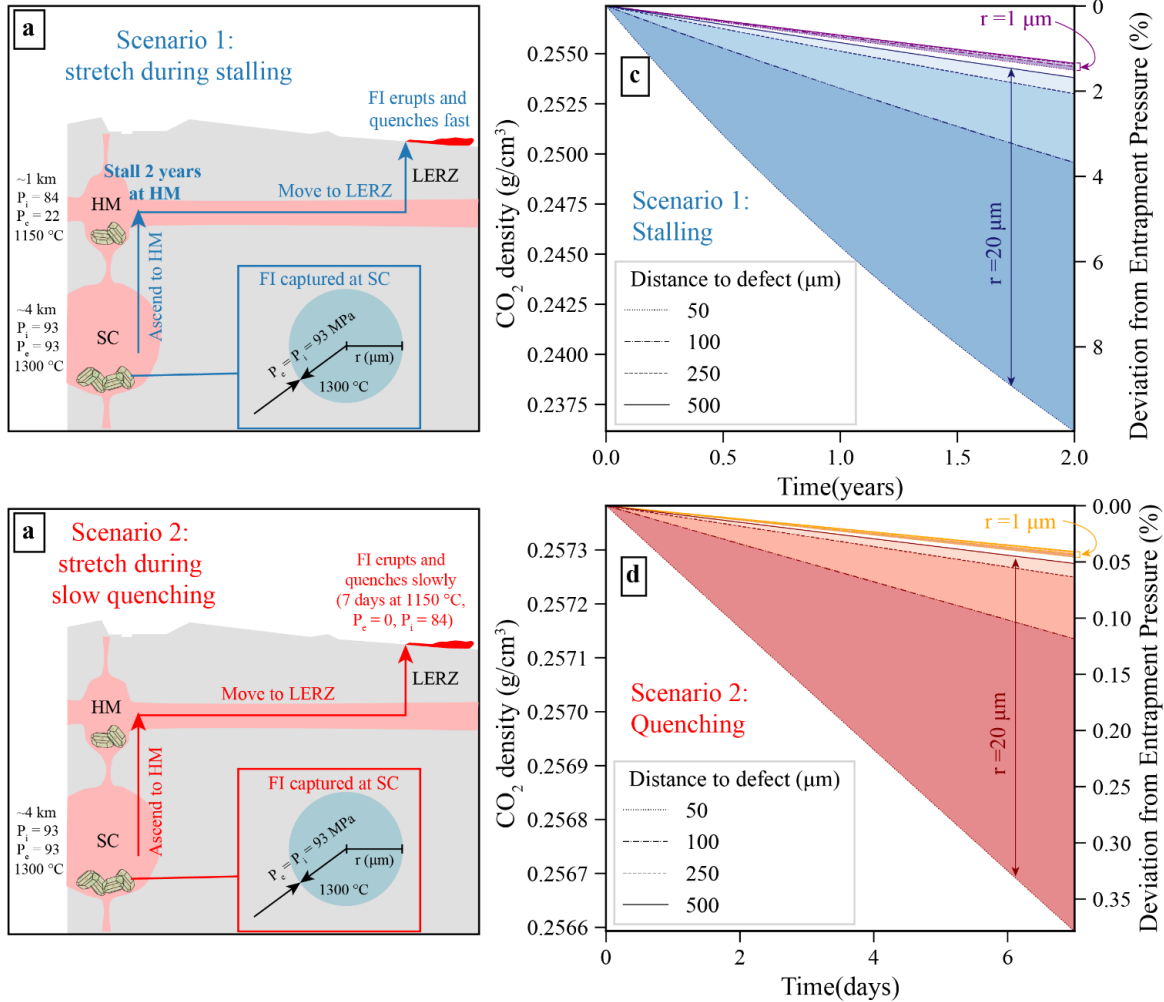
220

Figure 4: Assessing crystal cargoes and fluid inclusion re-equilibration. (a) Schematic diagram of Kīlauea plumbing system showing the scenario modelled in (b), where 1 and 20 μm radii fluid inclusions are captured in olivine crystals at the South Caldera (SC), they are transported to Halema'uma'u (HM) reservoir, almost immediately mobilized to the Lower East Rift Zone (LERZ), erupted, and slowly quenched for 7 days (T is kept at 1150 °C in the model). (b) Stretching model for slow quenching scenario (a). (c) Schematic diagram of Kīlauea plumbing system showing the scenario modelled in (d), where the magma stalls at Halema'uma'u (HM) reservoir for 2 years prior to eruption. (d) Stretching model for stalling scenario (c).

11

Conclusions

Here, we compare barometric estimates of magma storage depths for the 2018 LERZ eruption of Kīlauea volcano using CO_2-dominated fluid inclusions to those obtained via melt inclusion studies. We find that fluid inclusions captured at Kīlauea are unlikely to be significantly affected by re-equilibration on timescales relevant to magma storage and migration. Within uncertainty, they reflect the same entrapment depths as those recorded by melt inclusions in the same sample splits. Therefore, fluid inclusions are a suitable alternative to melt inclusion for barometry in shallow CO_2-dominated volcanic systems.

Author contributions

CLJD prepared the Fogo fluid inclusions, performed all Raman and Microthermometry analyses, developed the MC subsampling and fluid inclusion re-equilibration code, and wrote the manuscript. PW acquired the funding, prepared the Kilauea fluid inclusions, wrote the peak fitting/EOS code, and edited the manuscript.

Acknowledgements

Data availability

All data are made available with the publication. All data are also available on Github (https://github.com/cljdevitre/KilaueaMIFI2023) along with notebooks to reproduce figures published in the article, the notebooks for running the MC KS test simulations and data processing notebooks for DiadFit. The Github repo will be archived at Zenodo upon article acceptance. Documentation for the python3 tool (https://github.com/cljdevitre/RelaxiFI) developed to assess re-equilibration of FI is available at https://relaxifi.readthedocs.io/.

References

12

Roedder, E. (1979) Origin and significance of magmatic inclusions. *Bulletin de Minéralogie* 102, 487–510. *https://doi.org/10.3406/bulmi.1979.7299*.

260   Wanamaker, B.J., Evans, B. (1989) Mechanical re-equilibration of fluid inclusions in San Carlos olivine by power-law creep. *Contributions to Mineralogy and Petrology* 102, 102–111. *https://doi.org/10.1007/BF01160194*.

Span, R., Wagner, W. (1996) A new equation of state for carbon dioxide covering the fluid region from the triple-point temperature to 1100 K at pressures up to 800 MPa. *Journal of physical and chemical reference data*. 265   American Institute of Physics for the National Institute of Standards and … 25, 1509–1596.

Burke, E.A.J. (2001) Raman microspectrometry of fluid inclusions. *Lithos* 55, 139–158. *https://doi.org/10.1016/S0024-4937(00)00043-8*.

Newman, S., Lowenstern, J.B. (2002) VolatileCalc: a silicate melt–H2O–CO2 solution model written in Visual Basic for excel. *Computers & Geosciences* 28, 597–604. *https://doi.org/10.1016/S0098-3004(01)00081-4*.

270   Klügel, A., Hansteen, T.H., Galipp, K. (2005) Magma storage and underplating beneath Cumbre Vieja volcano, La Palma (Canary Islands). *Earth and Planetary Science Letters* 236, 211–226. *https://doi.org/10.1016/j.epsl.2005.04.006*.

Duan, Z., Zhang, Z. (2006) Equation of state of the H2O, CO2, and H2O–CO2 systems up to 10 GPa and 2573.15K: Molecular dynamics simulations with ab initio potential surface. *Geochimica et Cosmochimica Acta* 70, 275   2311–2324. *https://doi.org/10.1016/j.gca.2006.02.009*.

Hansteen, T.H., Klügel, A. (2008) Fluid Inclusion Thermobarometry as a Tracer for Magmatic Processes. *Reviews in Mineralogy and Geochemistry* 69, 143–177. *https://doi.org/10.2138/rmg.2008.69.5*.

Putirka, K.D. (2008) Thermometers and barometers for volcanic systems. *Reviews in mineralogy and geochemistry*. Mineralogical Society of America 69, 61–120.

280   Baker, S., Amelung, F. (2012) Top-down inflation and deflation at the summit of Kīlauea Volcano, Hawai'i observed with InSAR. *Journal of Geophysical Research: Solid Earth* 117. *https://doi.org/10.1029/2011JB009123*.

Iacono-Marziano, G., Morizet, Y., Le Trong, E., Gaillard, F. (2012) New experimental data and semi-empirical parameterization of H2O–CO2 solubility in mafic melts. *Geochimica et Cosmochimica Acta*. Elsevier 97, 285   1–23.

Kobayashi, T., Yamamoto, J., Hirajima, T., Ishibashi, H., Hirano, N., Lai, Y., Prikhod'ko, V.S., Arai, S. (2012) Conformity and precision of CO2 densimetry in CO2 inclusions: microthermometry versus Raman microspectroscopic densimetry. *Journal of Raman Spectroscopy* 43, 1126–1133. *https://doi.org/10.1002/jrs.3134*.

13

290   Zanon, V., Frezzotti, M.L. (2013) Magma storage and ascent conditions beneath Pico and Faial islands (Azores archipelago): A study on fluid inclusions. *Geochemistry, Geophysics, Geosystems* 14, 3494–3514. *https://doi.org/10.1002/ggge.20221*.

Poland, M.P., Miklius, A., Montgomery-Brown, E.K. (2014) Magma supply, storage, and transport at shield-stage Hawaiian volcanoes. *Characteristics of Hawaiian volcanoes*. US Geological Survey Reston, VA 1801,
295   179–234.

Shishkina, T.A., Botcharnikov, R.E., Holtz, F., Almeev, R.R., Jazwa, A.M., Jakubiak, A.A. (2014) Compositional and pressure effects on the solubility of H2O and CO2 in mafic melts. *Chemical Geology* 388, 112–129. *https://doi.org/10.1016/j.chemgeo.2014.09.001*.

Ghiorso, M.S., Gualda, G.A.R. (2015) An H2O–CO2 mixed fluid saturation model compatible with rhyolite-
300   MELTS. *Contributions to Mineralogy and Petrology* 169, 53. *https://doi.org/10.1007/s00410-015-1141-8*.

Anderson, K.R., Poland, M.P. (2016) Bayesian estimation of magma supply, storage, and eruption rates using a multiphysical volcano model: Kīlauea Volcano, 2000–2012. *Earth and Planetary Science Letters* 447, 161–171. *https://doi.org/10.1016/j.epsl.2016.04.029*.

305   Lamadrid, H.M., Moore, L.R., Moncada, D., Rimstidt, J.D., Burruss, R.C., Bodnar, R.J. (2017) Reassessment of the Raman CO2 densimeter. *Chemical Geology* 450, 210–222. *https://doi.org/10.1016/j.chemgeo.2016.12.034*.

Yuan, X., Mayanovic, R.A. (2017) An Empirical Study on Raman Peak Fitting and Its Application to Raman Quantitative Research. *Applied Spectroscopy*. Society for Applied Spectroscopy 71, 2325–2338.

310   Anderson, K.R., Johanson, I.A., Patrick, M.R., Gu, M., Segall, P., Poland, M.P., Montgomery-Brown, E.K., Miklius, A. (2019) Magma reservoir failure and the onset of caldera collapse at Kīlauea Volcano in 2018. *Science*. American Association for the Advancement of Science 366, eaaz1822. *https://doi.org/10.1126/science.aaz1822*.

Tucker, J.M., Hauri, E.H., Pietruszka, A.J., Garcia, M.O., Marske, J.P., Trusdell, F.A. (2019) A high carbon content
315   of the Hawaiian mantle from olivine-hosted melt inclusions. *Geochimica et Cosmochimica Acta* 254, 156–172. *https://doi.org/10.1016/j.gca.2019.04.001*.

Wieser, P.E., Vukmanovic, Z., Kilian, R., Ringe, E., Holness, M.B., Maclennan, J., Edmonds, M. (2019) To sink, swim, twin, or nucleate: A critical appraisal of crystal aggregation processes. *Geology* 47, 948–952. *https://doi.org/10.1130/G46660.1*.

320   DiBenedetto, M., Qin, Z., Suckale, J. (2020) Crystal aggregates record the pre-eruptive flow field in the volcanic conduit at Kīlauea, Hawaii. *Science Advances*. American Association for the Advancement of Science 6, eabd4850. *https://doi.org/10.1126/sciadv.abd4850*.

Klügel, A., Day, S., Schmid, M., Faria, B. (2020) Magma Plumbing During the 2014–2015 Eruption of Fogo (Cape Verde Islands). *Frontiers in Earth Science* 8.

14

325 Bakker, R.J. (2021) The perfection of Raman spectroscopic gas densimeters. *Journal of Raman Spectroscopy* 52, 1923–1948. *https://doi.org/10.1002/jrs.6245*.

Barker, A.K., Rydeblad, E.M., Silva, S.M.D.M. (2021) Magma Storage at Ocean Islands: Insights From Cape Verde. In: Masotta, M., Beier, C., Mollo, S. (eds) *Geophysical Monograph Series*. Wiley, 45–78. *https://doi.org/10.1002/9781119564485.ch3*.

330 DeVitre, C.L., Allison, C.M., Gazel, E. (2021) A high-precision CO2 densimeter for Raman spectroscopy using a Fluid Density Calibration Apparatus. *Chemical Geology* 584, 120522. *https://doi.org/10.1016/j.chemgeo.2021.120522*.

Hagiwara, Y., Yoshida, K., Yoneda, A., Torimoto, J., Yamamoto, J. (2021) Experimental variable effects on laser heating of inclusions during Raman spectroscopic analysis. *Chemical Geology* 559, 119928.
335 *https://doi.org/10.1016/j.chemgeo.2020.119928*.

Lerner, A.H., Wallace, P.J., Shea, T., Mourey, A.J., Kelly, P.J., Nadeau, P.A., Elias, T., Kern, C., Clor, L.E., Gansecki, C. (2021) The petrologic and degassing behavior of sulfur and other magmatic volatiles from the 2018 eruption of Kīlauea, Hawai'i: melt concentrations, magma storage depths, and magma recycling. *Bulletin of Volcanology*. Springer 83, 1–32.

340 Wieser, P.E., Lamadrid, H., Maclennan, J., Edmonds, M., Matthews, S., Iacovino, K., Jenner, F.E., Gansecki, C., Trusdell, F., Lee, R.L., Ilyinskaya, E. (2021) Reconstructing Magma Storage Depths for the 2018 Kīlauean Eruption From Melt Inclusion CO2 Contents: The Importance of Vapor Bubbles. *Geochemistry, Geophysics, Geosystems* 22, e2020GC009364. *https://doi.org/10.1029/2020GC009364*.

Allison, C.M., Roggensack, K., Clarke, A.B. (2022) MafiCH: a general model for H2O–CO2 solubility in mafic
345 magmas. *Contributions to Mineralogy and Petrology* 177, 40. *https://doi.org/10.1007/s00410-022-01903-y*.

Wieser, P.E., Iacovino, K., Matthews, S., Moore, G., Allison, C.M. (2022) VESIcal: 2. A Critical Approach to Volatile Solubility Modeling Using an Open-Source Python3 Engine. *Earth and Space Science* 9, e2021EA001932. *https://doi.org/10.1029/2021EA001932*.

350 Dayton, K., Gazel, E., Wieser, P., Troll, V.R., Carracedo, J.C., La Madrid, H., Roman, D.C., Ward, J., Aulinas, M., Geiger, H., Deegan, F.M., Gisbert, G., Perez-Torrado, F.J. (2023) Deep magma storage during the 2021 La Palma eruption. *Science Advances*. American Association for the Advancement of Science 9, eade7641. *https://doi.org/10.1126/sciadv.ade7641*.

DeVitre, C.L., Gazel, E., Ramalho, R.S., Venugopal, S., Steele-MacInnis, M., Hua, J., Allison, C.M., Moore, L.R.,
355 Carracedo, J.C., Monteleone, B. (2023) Oceanic intraplate explosive eruptions fed directly from the mantle. *Proceedings of the National Academy of Sciences*. Proceedings of the National Academy of Sciences 120, e2302093120. *https://doi.org/10.1073/pnas.2302093120*.

Mourey, A.J., Shea, T., Costa, F., Shiro, B., Longman, R.J. (2023) Years of magma intrusion primed Kīlauea Volcano (Hawai'i) for the 2018 eruption: evidence from olivine diffusion chronometry and monitoring
360 data. *Bulletin of Volcanology* 85, 18. *https://doi.org/10.1007/s00445-023-01633-4*.

15

Wieser, P.E., DeVitre, C.L. (2023) DiadFit: An Open-SourcePython3 Tool for Peak fitting of Raman Data from silicate melts and CO2 fluids. EarthArXiv*https://doi.org/10.31223/X5CQ1F*.

Wieser, P.E., Kent, A.J.R., Till, C.B., Donovan, J., Neave, D.A., Blatter, D.L., Krawczynski, M.J. (2023) Barometers Behaving Badly I: Assessing the Influence of Analytical and Experimental Uncertainty on Clinopyroxene Thermobarometry Calculations at Crustal Conditions. *Journal of Petrology* 64, egac126. *https://doi.org/10.1093/petrology/egac126*.

365

Reliability of Raman analyses of CO_2-dominated fluid inclusions as a geobarometer at Kīlauea

Charlotte L. DeVitre, Penny E. Wieser

Supplementary Information

The Supplementary Information includes:

- ➢ 1. Detailed materials and methods
- ➢ 2. Statistical significance of the MI vs FI recorded pressures
- ➢ 3. Fluid % effect on calculated densities and pressures
- ➢ Figures S-1 to S-10. Figures are included in the text where relevant.
- ➢ Dataset S-1 (Excel Table attached to the submission)
- ➢ Image Database S-1 (PDF attached to the submission)
- ➢ Supplementary Information References

All raw data, including spectra, fitting images and Jupyter Lab notebooks to process and plot data can be found on the Github repository https://github.com/cljdevitre/KilaueaMIFI2023, which will be archived at Zenodo upon publication.

1. Detailed materials and methods

1.1 Samples

Olivines from three samples of the 2018 LERZ eruption of Kīlauea volcano in Hawai'i (Fissure 8 samples of May, July and August 2018) were picked under a binocular microscope, and individually mounted in CrystalBond™ on glass slides from jaw crushed and sieved samples as described in (Wieser *et al.*, 2021) . The May 2018 sample erupted on May 30, 2018 (Lab code LL4, USGS code KE62–3293), as vesicular reticulite and scoria; The July 2018 sample erupted in mid-July, 2018 (Lab code LL8, no USGS code) was

sampled from the selvages of a naturally quenched, and highly vesicular proximal overflow from the Fissure 8 channel; The August 2018 sample erupted on August 1st, 2018 (Lab code LL7, USGS code KE62–A3321F) and was sampled directly from the channel and rapidly quenched in water (Wieser *et al.*, 2021). FI were revealed by grinding using 250–3,000 grade wet and dry paper. Petrographic work was done to describe the emplacement of FI and FIA in the crystals. Photos were taken of the crystals and FI (see Image Database S-1). Additionally, FI were located and photographed in the same crystals as those in which melt inclusions were analyzed in (Wieser *et al.*, 2021). In total we analyzed 145 FI hosted in 57 olivine crystals 2018 LERZ eruption of Kīlauea volcano. In the final dataset (102 fluid inclusions), we discarded spectra that yielded density errors >20% due to poor spectral quality (e.g., high and/or wavy backgrounds, low signal/noise ratio) and excluded fluid inclusions with a melt film that occupied more than 20% of the inclusion volume.

Olivines from tephra of the 1951 eruption of Fogo Volcano in Cabo Verde (DeVitre *et al.*, 2023), were also picked under binocular microscope and individually mounted in CrystalBond™. FI were revealed by grinding using 600-2000 grit wet paper and polish refined using 1 and 0.3 um wet paper and alumina paste. These crystals were doubly polished for micro thermometric analyses. We analyzed 63 FI in 12 crystals of this eruption via Raman and microthermometry in two weeks.

1.2 Raman spectroscopy FI CO_2

We collected Raman spectra using a WiTec Alpha 300R Raman spectrometer at the Department of Earth and Planetary Sciences at the University of California, Berkeley. We use a green solid state 532.046 nm laser focused as an excitation source with a 50x objective (x0.55NA, 9.1 mm focal distance) and 100x objective (x0.95NA, 4mm WD). The system is equipped with TruePower system which allows for in-fiber power adjustments of <0.1 mW. We used a power of 6-12 mW. We used an FDCA built following the method of (DeVitre *et al.*, 2021)with an extended upper pressure limit from 35 to up to 68 MPa (through use of a sapphire window instead of fused silica-quartz) to produce calibration equations relating CO_2 density and Δ_{CO_2} for our instrument. These equations are available in DiadFit (Wieser and DeVitre, 2023) and have the same functional form as those reported in (DeVitre *et al.*, 2021) with updated coefficients.

Spectra for FI were collected at 37 °C, with temperature regulated at 37°C using a Peltier thermoelectric stage with a center hole fixed on a magnetic aluminum holder. Spectra were acquired with five accumulations of 45 s of integration time (total analytical time = 225 s) in a single window using 1800 grooves/mm (~0.54 cm^{-1} spectral resolution) and a spectral center of 1325 cm^{-1}. We discarded spectra with less than 3 points above the background (these yield spurious fits with up to >100% error on fitting), those with high backgrounds interfering with the fit and those with normalized Intensity/FWHM <200 according to the criteria of (Yuan and Mayanovic, 2017) as these cannot be fit confidently. A filtered total of 124 FI yielded results with 1σ in CO_2 density better than ~0.02 g/mL (Data Table S-1)

Neon (Ne) spectra were collected every ~10-15 minutes using the same grating and spectral center as the unknown and three accumulations of 45 s integration time, to correct for non-linearity of the Raman shift axis (Lin *et al.*, 2007; Wang *et al.*, 2011; Lamadrid *et al.*, 2017; DeVitre *et al.*, 2021).

All spectra were processed using Python tool DiadFit v0.0.62 (Wieser and DeVitre, 2023). Spectra are baseline-subtracted prior to fitting (2nd degree polynomial baseline subtraction anchored on either side of peak of interest), and we fit a Pseudo-Voigt peak (mixed Gaussian and Lorentzian model) on each main CO_2 peak (1285 cm^{-1} and 1389 cm^{-1}).Voigt and Pseudo-Voigt functional forms are typically considered the most appropriate for symmetric Raman peaks (e.g., single-phase CO_2 peaks and Neon emission lines, Yuan and Mayanovic, 2017). For fitting, CO_2 spectra were separated into 3 groups based on overall intensity of the spectra, and overlap between main peaks, hot bands (1270 cm^{-1} and 1410 cm^{-1}) and ^{13}C (1370 cm^{-1}) such that additional peaks were simultaneously fit when needed to reduce the effect of residuals on the fit (Jupyter notebooks are included in the supplement). We correct our data following the methods of (Lamadrid *et al.*, 2017; DeVitre *et al.*, 2021) using two known Ne emission lines (1115.9919 cm^{-1} and 1446.4696 cm^{-1}) that

encompass the Fermi diad. A single Voigt peak is fit at 1446-1453 cm^{-1} for the upper line while two Voigt peaks (1113-1120 cm^{-1} and 1115-1122 cm^{-1}) are used for the lower line since it appears as a double-peak at out spectral resolution. We calculate the instrumental drift correction factor Ne_{coeff} as shown in Eq. 1):

$$Ne_{coeff} = \left(\frac{\Delta Ne_{known}}{\Delta Ne_{observed}} \right) \qquad\qquad (1)$$

where ΔNe_{known} is the theoretical separation of the Ne emission lines in air and $\Delta Ne_{observed}$ is the measured separation of the same Ne emission lines on the Raman spectrum.

We then model the instrumental drift during each session as a polynomial function (typically 1st to 3rd degree polynomial, unless large temperature fluctuations happened during the session) relating Ne_{coeff} to time in seconds. Exact timestamps are extracted for each CO_2 spectrum and the appropriate Ne_{coeff} from the model is applied to correct the separation of the Fermi Diad. We also fit and calculated areas for SO_2 and CO_3 when observed on the spectra, these are fit as gaussian functions.

We calculate densities using the appropriate calibrated density equations for our instrument using DiadFit (Wieser and DeVitre, 2023). We estimate entrapment temperatures from the Fo content of the olivine (see below). We then calculate pressures from measured densities and estimated entrapment temperatures using the EOS of Span and Wagner, (1996) and propagate uncertainty using Monte Carlo simulations. Finally, we calculate the depths of entrapment using the crustal density model of Ryan, (1987), described in Lerner *et al.*, (2021) for Hawai'i.

1.3 Quantifying uncertainty and reproducibility of measurements of fluid inclusions

Uncertainties on fluid inclusion pressures are propagated in DiadFit, using Monte Carlo simulations considering 50 K uncertainty on the Temperature (see section 1.5) and 1σ uncertainty on density from peak-fit uncertainties on CO_2 spectra and the uncertainty in the Ne correction model estimated by DiadFit. The majority of data presented in the paper was fitted with DiadFit version v0.0.62. This version propagates the uncertainty in peak position into calculated densities. A newer version of DiadFit (v0.0.78) that was released recently also accounts for the error from the densimeter and drift correction model. To assess differences between these errors, we refit a subset of Raman data (October 17th 2022; see data repository) that encompasses most CO_2 densities found in our study (Wieser and DeVitre, 2023). We did not apply filters for bad spectra (e.g., high background, too little intensity/ number of points to fit) for this exercise. It is immediately apparent that the error for our measurements predominantly arises from the error involved in fitting Diad peaks (Fig. S-1), and that the error on the densimeter and Ne line correction plays only a minor role in most cases (Fig. S-1c and d; <10%). Additionally, the densities and associated errors calculated by version v0.0.62 are not significantly different from those calculated by v0.0.78 (Fig. S-2), and both lie on a 1:1 line. The densities calculated densities with v.0.078 are within 0.004 g/cm^3 of those calculated with v.0.062 and except for 4 data points, the majority are within 0.001 g/cm^3. The calculated errors are for the most part within 0.002 g/cm^3 except for 2 points (one at 0.004 g/cm^3 and one at 0.01 g/cm^3). We note that these two datapoints as well as some others were discarded in the final dataset due to low intensity and/or high backgrounds which largely accounts for the high fitting error. Overall, this shows that for the samples examined in this study, the peak fitting errors from v0.0.62 are a reasonable estimate, and complete refitting of the dataset is not justified.

We also assess the reproducibility of our measurements based on repeated analyses of single fluid inclusions (Fig. S-3). For repeated measurements, the standard deviation is no higher than 0.02 g/cm^3, even when the measurements were repeated on different days (Fig. S-3 a and b). Further, the 1σ error output from DiadFit is similar to the standard deviation of repeated measurements and is often slightly higher. Overall, only one measurement in our reported dataset has a 1σ > 0.02 g/cm^3, which indicates that the use of a CO_2 density error of ~0.02 g/cm^3 in the Monte Carlo error simulations is appropriate to describe the error in our dataset. This also matches the findings of Dayton *et al.* (2023) based on their repeated measurements using identical instrument and calibration hardware.
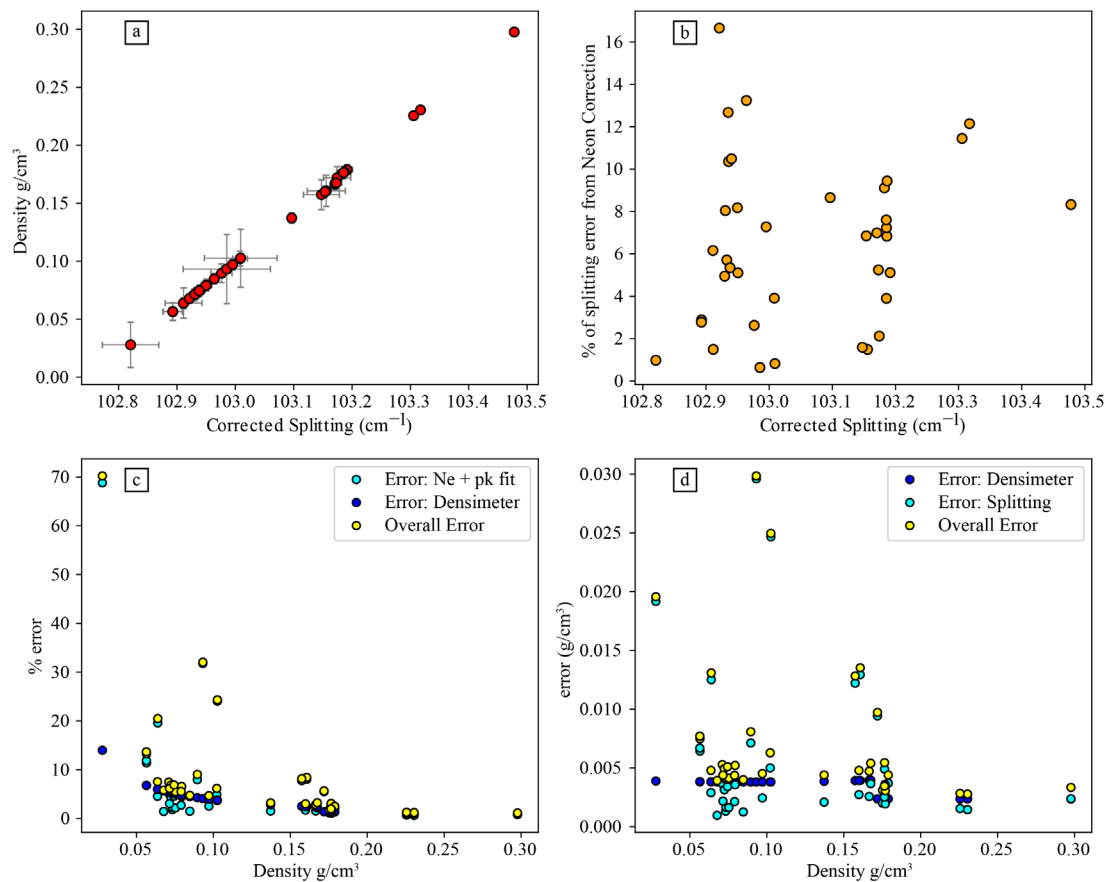
Figure S-1. Refit Raman data from October 17th 2022 using DiadFit v. 0.0.78. (a) Separation of the Fermi Diad vs CO_2 density with error bars shown in black. (b) Percentage of the error on the Fermi Diad separation that is due to the Neon Correction. (c) Percentage of error in CO_2 density vs CO_2 density. Yellow dots are the overall error (from all sources), cyan dots are the error from peak fittin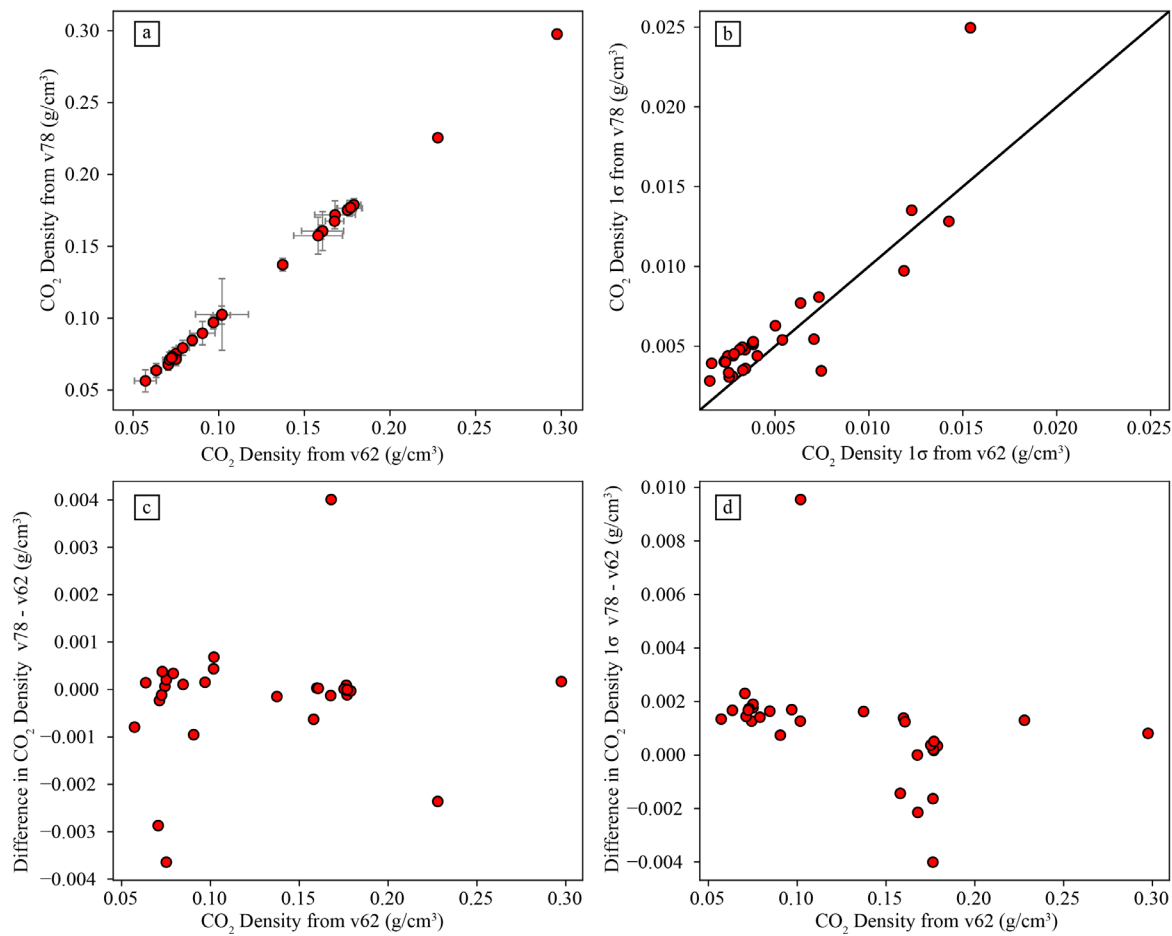g and neon correction alone and blue dots are the error from the densimeter only. (d) Absolute error in CO_2 density vs CO_2 density. Yellow dots are the overall error (from all sources), cyan dots are the error from peak fitting and neon correction alone and blue dots are the error from the densimeter only.

Figure S-2. Refit Raman data from October 17th 2022 using DiadFit v0.0.78 vs original data fit using DiadFit v0.0.62 (a) CO_2 density from version v0.0.78 vs from version v0.0.62 with error bars shown in black. (b) CO_2 density 1σ error from version v0.0.78 vs from version v0.0.62. (c) Difference in CO_2 density from v78 and CO_2 density from v62. (d) Difference in CO_2 density 1σ error from v78 and CO_2 density 1σ from v62.
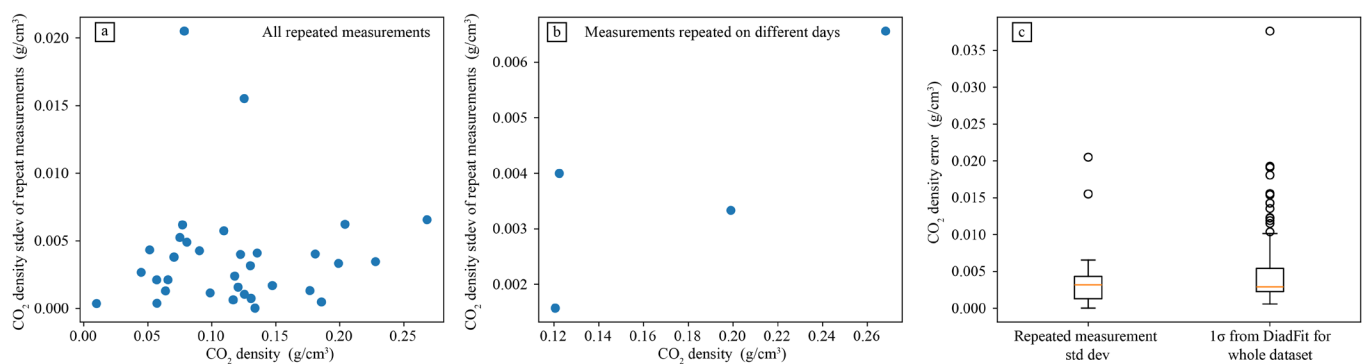
Figure S-3. Comparison of error from DiadFit and reproducibility of repeated measurements. (a) Standard deviation of repeated measurements vs CO_2 density. This plot includes measurements that were repeated on the same day (consecutive repeated measurements) as well as those that were repeated on a different day. (b) Standard deviation of repeated measurements vs CO_2 density considering only measurements with repeats on different days (for the same fluid inclusion at least one of the repeats was on a different day). (c) Box plots of CO_2 density error for two groups: repeated measurements (this is the standard deviation of N repeated measurements) and the reported error calculated

from DiadFit. This demonstrates the error estimated by DiadFit is a good match to the error determined by repeated measurements.

1.4 Microthermometry of FI

For samples with bulk CO_2 densities above the critical density of CO_2 (~0.44 g/mL), we conducted micro thermometry experiments to obtain the freezing and homogenization temperatures and calculate an independent estimate of the CO_2 density of the FI. It was not possible to obtain microthermometric data for FI that homogenize to vapor, as it is difficult to observe the homogenization of the thin liquid film into vapor in our samples. These experiments were conducted using a Linkam THMSG600 heating and freezing stage, with environmental control from -195 ˚C to 600 ˚C, equipped with a liquid nitrogen cooling pump allowing for cooling rates from 0.01 to 150 ˚C/min. We used pure CO_2-H_2O standards to calibrate temperature. All experiments were done using the cycling technique (Hansteen and Klügel, 2008) to ensure that homogenization was completed. We then converted the homogenization temperatures to CO_2 density using the EOS of (Span and Wagner, 1996) implemented in DiadFit (Wieser and DeVitre, 2023). All FI were found to have melting temperatures -56.5 ˚C ±0.1 ˚C (Fig. S-4a), indicating that they are pure CO_2.
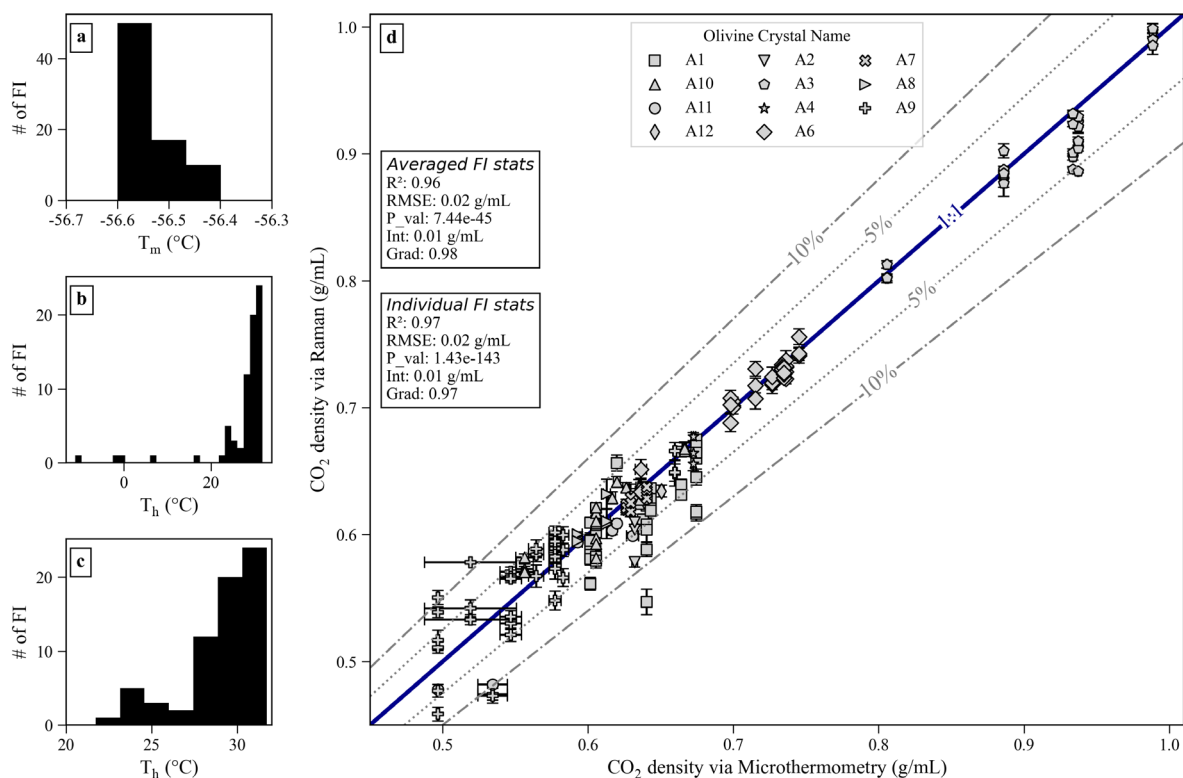
Figure S-4. CO_2 **densities via microthermometry versus calibrated Raman Spectroscopy. (a) Freezing temperatures of FI. (b) Homogenization temperatures of FI (all FI homogenized to liquid). (c) close-up of panel b (d) Density via Raman vs density via micro thermometry. FIs in the same crystal are plotted with the same symbol. Error bars for Raman-based** CO_2 **densities are propagated fitting + Neon correction uncertainties while error bars for microthermometry are the standard deviation of homogenization temperatures obtained during cycling.**

Under Raman spectroscopy, none of the FI analyzed had detectable amounts of any other gases, however they contained variable amounts of carbonate. Homogenization temperatures ranged from –11.1 ±0.2 ˚C to 31.6 ±1 ˚C (Fig S-1b-c), measurements with homogenization temperatures close to critical were more

difficult to perform and the uncertainty on the temperature is therefore higher, limited by the high $\Delta\rho/\Delta T$ and the accuracy of the temperature controller of the stage. Peak-fitting and drift and precision account for most of the uncertainty for Raman (See Fig. 8,Wieser and DeVitre, 2023), while the uncertainty for microthermometry can be attributed to difficulty in observing the phase homogenization near and/or below the critical density of CO_2, thermocouple accuracy and precision of thermal control. For densities close to critical (~0.44 g/mL), the uncertainty on microthermometry measurements significantly increases due to much higher $\Delta\rho/\Delta T$ – such that very small uncertainties in the homogenization temperature can cause much larger uncertainties in the density (Hansteen and Klugel, 2008).

1.5 Host olivine chemistry

Spot analyses of host olivines were conducted using a JEOL JXA-8230 EPMA in the Mineral and Microchemical Analysis Facility at Stanford University. Counting statistics and other analytical conditions along with repeated analyses of secondary standards (San Carlos Olivine, Stillwater olivine; (Jarosewich *et al.*, 1980) are presented in the Supporting Information (Data Table S-5).

Entrapment temperatures were estimated from the host olivine Fo content by developing an olivine-only thermometer suitable for Kilauea. The Fo content of an olivine is a function of the MgO and FeOt content of the liquid from which it equilibrates with, the Ol-Liq partition coefficient, and the proportion of Fe^{3+} in the liquid. Fortunately, Ol-saturated liquids at Kilauea have a relatively constant FeO content (See Fig. S-5, compiled glass data from (Clague and Bohrson, 1991; Clague *et al.*, 1995; Helz *et al.*, 2014, 2015; Sides *et al.*, 2014a, 2014b; Wieser *et al.*, 2019, 2021). Thus, if the Fo content is known, the K_D is known, the Fe^{3+} ratio is known, and the FeOt content can be relatively constant, the Fo content can be related to MgO, which in turn, can be related to temperature at Kilauea.
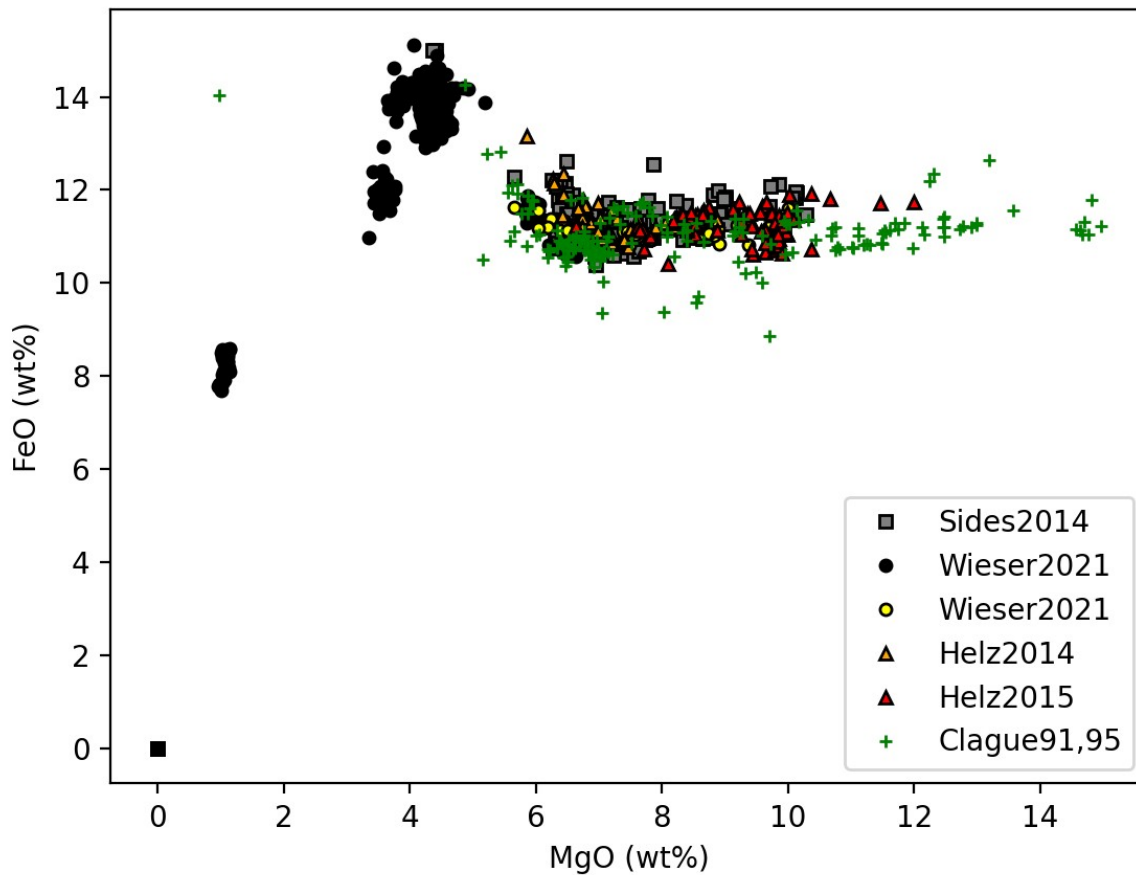
Figure S-5:   Compiled glass data used to calibrate an Ol-only thermometer.

To calibrate the Ol-only thermometer, we calculate a liquid-only temperature using the new MgO-thermometer of (Shea *et al.*, 2022) for each liquid in our compiled dataset. We also calculate an equilibrium olivine content using the K_D model of (Shea *et al.*, 2022), assuming $Fe^{3+}/Fe_T=0.15$ (Moussallam *et al.*, 2016; Helz *et al.*, 2017; Lerner *et al.*, 2021). We then fit a 3rd degree polynomial between temperature and Ol Fo content (Fig. S-6). We also show the polynomial that would result from using $Fe^{3+}/Fe_T=0.2$ instead. This is well within the ±50 K uncertainty used for temperature for the Monte-Carlo simulations (red dashed lines).
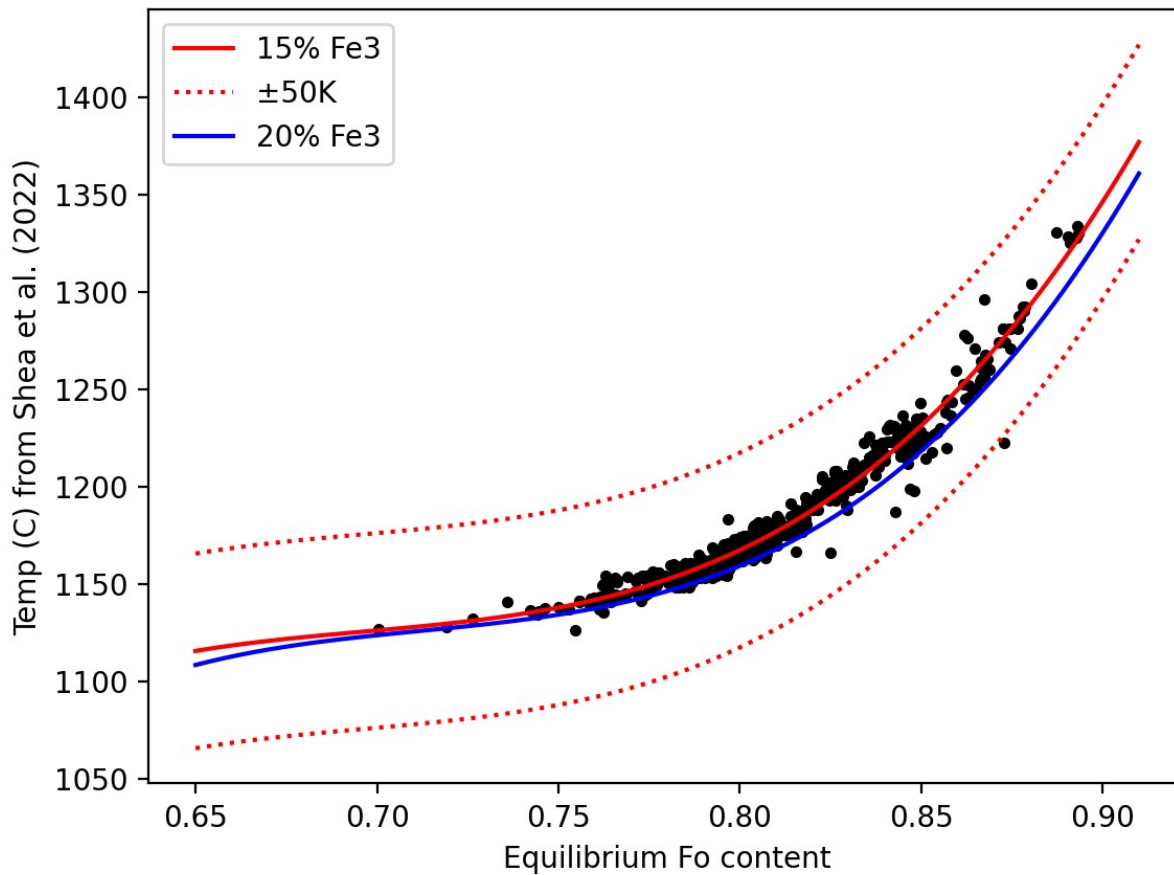
Figure S-6: 3rd degree polynomial fitted between equilibrium Fo content and temperature calculated from the glass composition using the thermometer of (Shea *et al.*, 2022).

We test the success of this Ol-only thermometer on the experimental data used to calibrate the expressions of (Shea *et al.*, 2022). We note that these experimental liquids have far more diversity in FeO content than natural Kilauea liquids, which explains the larger discrepancies that exist. If we restrict comparison to liquids within the mean±1σ of the observed distribution of Kilauean liquids, we can see the method is successful within the ±50K uncertainty allocated for Monte Carlo methods (pink box, Fig. S-7).
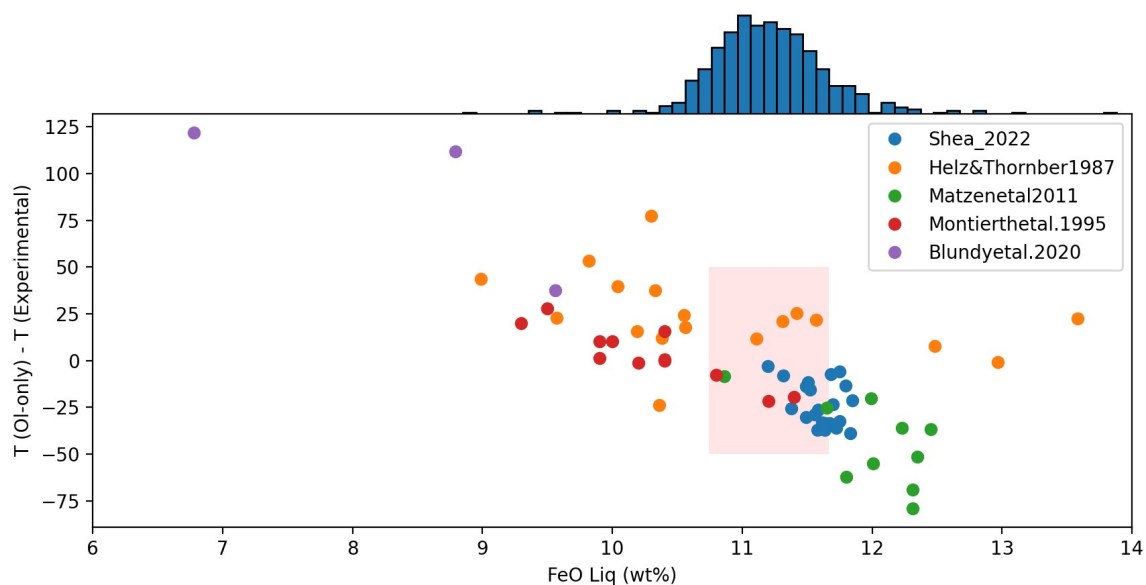
Figure S-7:   Assessing the Ol-only thermometer on the calibration dataset of (Shea *et al.*, 2022). The distribution of FeO contents in natural Kilauea liquids is shown with the blue histogram. In the red shaded box, we highlight experimental liquids within the mean±1σ of this distribution. These experiments lie well within the 1 σ=50K uncertainty allocated for entrapment temperatures.

1.6. Estimating SO₂/CO₂ ratios in FI

To estimate the SO_2 fraction in our FI, we calculated the area under the SO_2 peak (~1151 cm^{-1}). We first background subtracted using the same method as for CO_2 and Neon spectra and then fit a spline to the SO_2 spectrum. We then calculated the SO_2 mol % in the FI using the method of (Burke, 2001). We assumed the same instrument efficiency and use the coefficients presented in (Burke, 2001) for CO_2 and SO_2,

2. Statistical significance of the MI vs FI recorded pressures

To assess whether the pressures recorded by MI and FI are statistically different, we conducted Kolmogorov–Smirnov tests (KS). Given the relatively small sample set sizes (N<50), we perform both sample KS tests and Monte-Carlo KS tests using a Python3 routine in which we resampled 1000 times considering the uncertainties of each independent measurement. We compare the MI distributions for MI saturation pressures calculated using 5 different volatile solubility models (MagmaSat, Shishkina, MafiCH, VolatileCalc and Iacono-Marziano (Newman and Lowenstern, 2002; Iacono-Marziano *et al.*, 2012; Shishkina *et al.*, 2014; Ghiorso and Gualda, 2015; Allison *et al.*, 2022) with the pressure distribution from our new FI data (Fig. S-8). We note that there are very large variations in the MI saturation pressures when using different solubility models, which by themselves can largely account for the difference in the distributions (Fig. S-9). If one considers the MagmaSat solubility model, while the sample KS statistics appear significant (which would suggest that the FI are underestimating the magma storage pressures), when we consider the uncertainty on

10

both the FI and particularly the MI measurements, the Monte-Carlo KS statistic is no longer significant for any of the 3 events. This suggests that the FI are predicting the same entrapment pressures as the MI, within the uncertainty of the measurements.
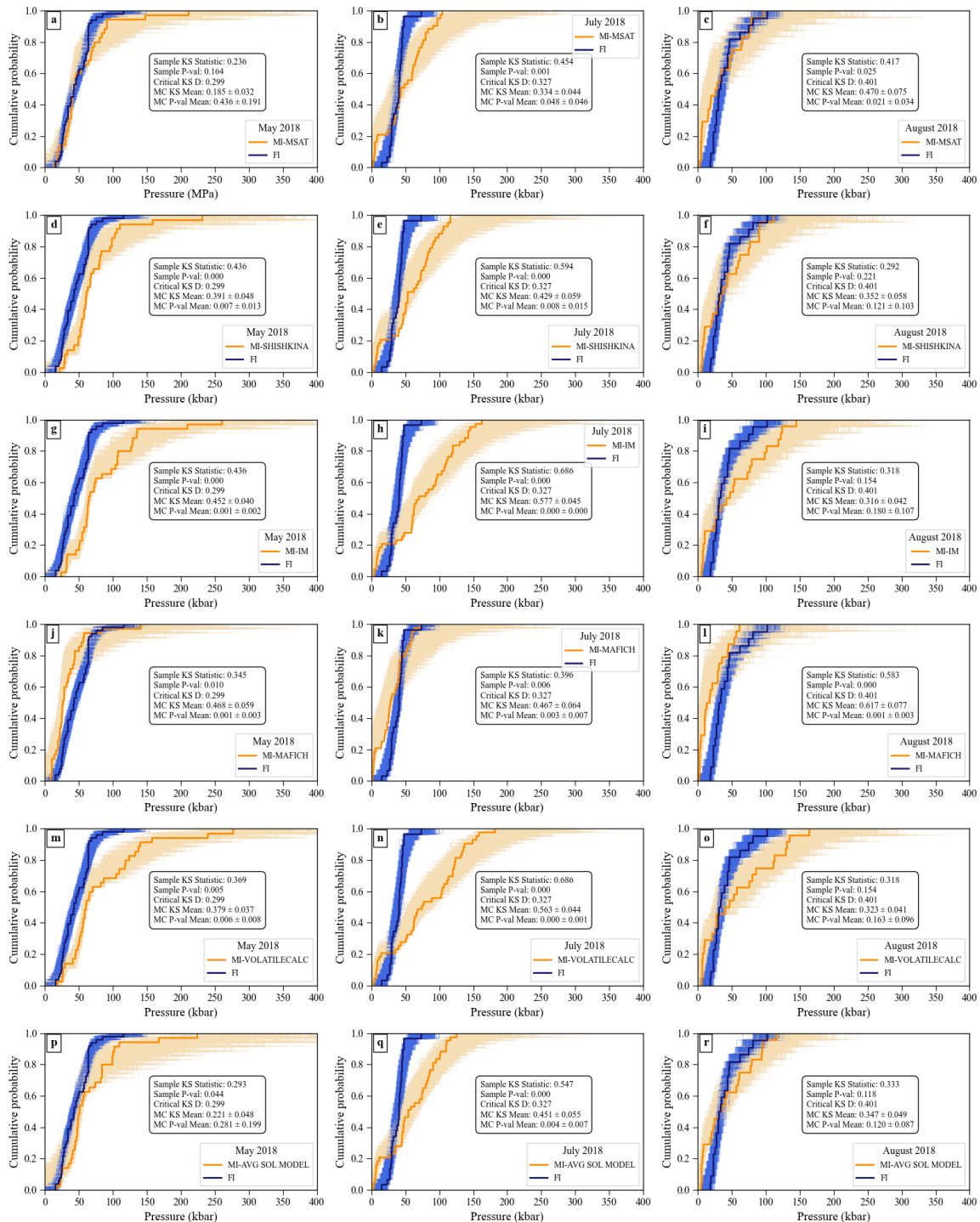
Figure S-8: Monte-Carlo KS tests on Cumulative distributions of pressures for FI (blue) and MI (orange) using different solubility models for each eruptive event. (a-c) MagmaSat. (d-f) Shishkina. (g-i) Iacono-Marziano. (j-l) MafiCH (m-o) VolatileCalc (p-r) Average Solubility model (standard deviation as uncertainty).
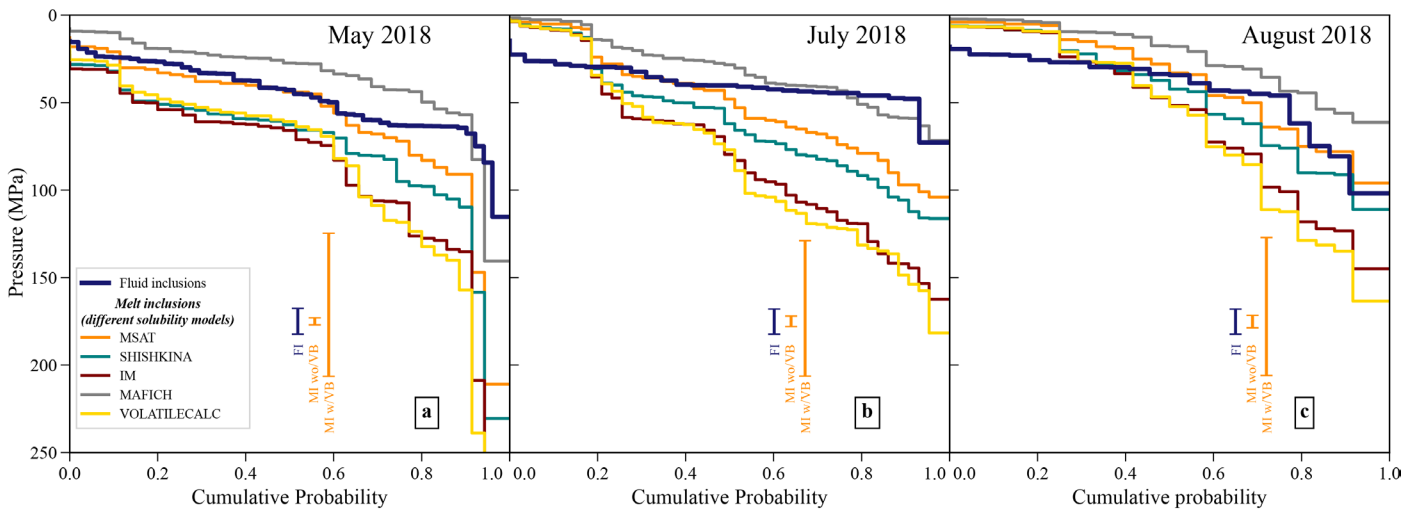
Figure S-9: Pressure CDF for comparing fluid and melt inclusion pressures for May 2018 (a), July 2018 (b) and August 2018 (c) using 5 different solubility models: MagmaSat (MSAT), Shishkina (SHISHKINA), Iacono-Marziano (IM), MafiCH (MAFICH), VolatileCalc (VOLATILECALC) (Newman and Lowenstern, 2002; Iacono-Marziano et al., 2012; Shishkina et al., 2014; Ghiorso and Gualda, 2015; Allison et al., 2022).

3. Effect of H₂O mol% in fluid on calculated densities and pressures

In relatively shallow systems like Kilauea, the exsolved vapour phase will not be pure CO_2, but will contain some fraction of H_2O. When performing fluid inclusion studies on mixed fluids, it is generally assumed that the H_2O has been lost from the fluid inclusion. Then, the measured CO_2 density is corrected based on the molar fraction of H_2O and molar ratios (see Hansteen and Klügel, 2008). This bulk density is then entered into a mixed H_2O-CO_2 equation of state to calculate pressure.
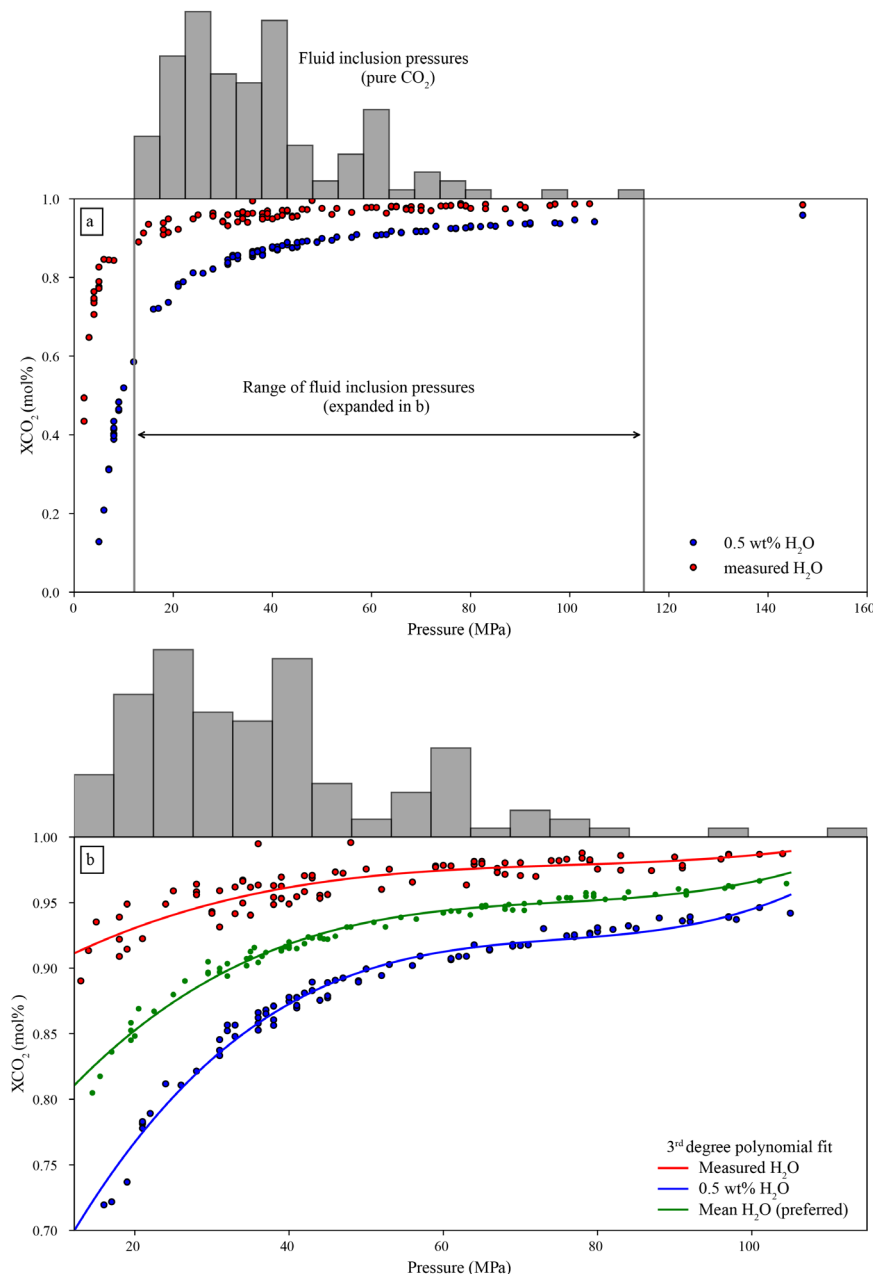
Fig S-10: XCO_2 values from (Wieser *et al.*, 2021). a) shows the entire range of measured pressures, while b) shows a zoomed in view looking at only the pressure range observed in fluid inclusions along with 3rd degree polynomial fits. Based on inferences of H_2O drainback and degassing (Lerner *et al.*, 2021). We use XCO_2 shown by the green polynomial, although we consider the uncertainty introduced by XCO_2 between the red

and blue polynomials (measured H_2O contents, red dots, lower plausible limit), and upper limit Kilauea H_2O contents (blue dots, 0.5 wt%, upper plausible limit).

To estimate the mol fraction of H_2O in the exsolved fluid, we examine melt inclusion data from (Wieser *et al.*, 2021). The solubility model MagmaSat returns the calculated pressure, and XH_2O at the point of vapour saturation. For the 2018 eruption, it is difficult to estimate the initial H_2O content at the time of melt and fluid inclusion entrapment, because H_2O was reset through diffusive re-equilibration with the carrier melt transporting crystals down the East Rift Zone. However, it has been suggested that the reservoir melts were likely drier than normal Kīlauea magmas due to mixing and degassing of summit lake lavas over the decade prior (Lerner *et al.*, 2021). To encompass this uncertainty, we show XH_2O calculated using the measured H_2O content, and 0.5 wt% H_2O, which encompasses the higher end of the range at Kīlauea over the last few hundred years (Fig. S-10, red and blue dots respectively). We also calculate the mean of the two (Fig. S-10b, green dots).

To perform the correction, we regress pressure vs. XCO_2 (equivalent to $1-XH_2O$) using a 3rd degree polynomial (Fig. S-10b) for measured H_2O contents, 0.5 wt% H_2O and the mean H_2O values. This means for each fluid inclusion we can allocate an approximate XH_2O value as $XH_2O = 1-XCO_2$. We then calculate pressure using the mixed CO_2-H_2O EOS of Duan and Zhang (2006) implemented in DiadFit v0.0.80. Given that our initial pressures were calculated using a pure CO_2 EOS, we iterate 4 times to converge towards a final corrected pressure. We note that the corrected pressures and associated uncertainties are within the pure CO_2 pressures and the uncertainty estimated by the Monte Carlo simulations (Fig. S11). We use the XCO_2 value from the green (middle) scenario, but consider the uncertainty introduced by XCO2 values between the blue and red lines.
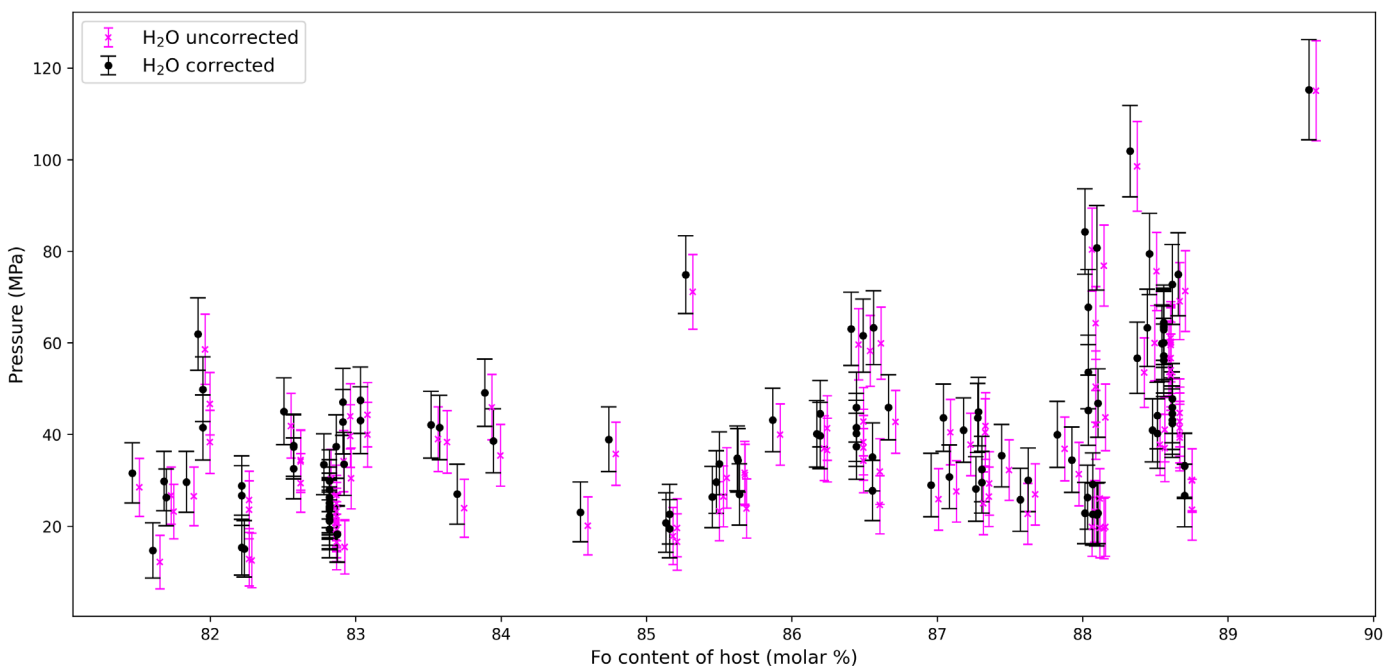

Fig S-11: Fluid inclusion pressures as a function of the Fo content of the olivine hosts. Black markers are H_2O corrected pressures, with corresponding uncertainties considering the minimum and maximum water content ranges from Fig. S10 as well as the uncertainty from the MonteCarlo simulations for the pure CO_2 EOS pressures, summed in quadrature. Magenta markers show the pure CO_2 EOS pressures and are artificially offset in Fo content by 0.05 to aid visibility.

4. Fluid % effect on calculated densities and pressures

Magmatic fluid inclusions are often trapped with variable small amounts of silicate melt. We estimated the proportion of exsolved fluid to silicate melt using FIJI (Schindelin *et al.*, 2012). We filtered out of the dataset any inclusion <80% exsolved fluid. In Fig S-12 and S-13, we plot the measured CO_2 density of FI in the same crystals, which have variable amounts of exsolved fluid. We also individually plot the FI in each crystal in subsequent panels. We found no clear trends indicating that FI with small amounts of silicate melt (<20%) are likely to record the same conditions as those with nearly no melt at all. Some crystals show a weak relationship where FI with no melt or very little melt have record the highest densities. However, we recognize the dataset is much too small to conclude on this matter. Future work is required to constrain whether any significant relationship exists. For this study, we consider that FI with >80% exsolved fluid offer a suitable record of pressure. This is consistent with previous work indicating that exchange of CO_2 with the melt is negligible in inclusions that trap predominantly the vapor phase (little melt) (Steele-MacInnis *et al.*, 2017).
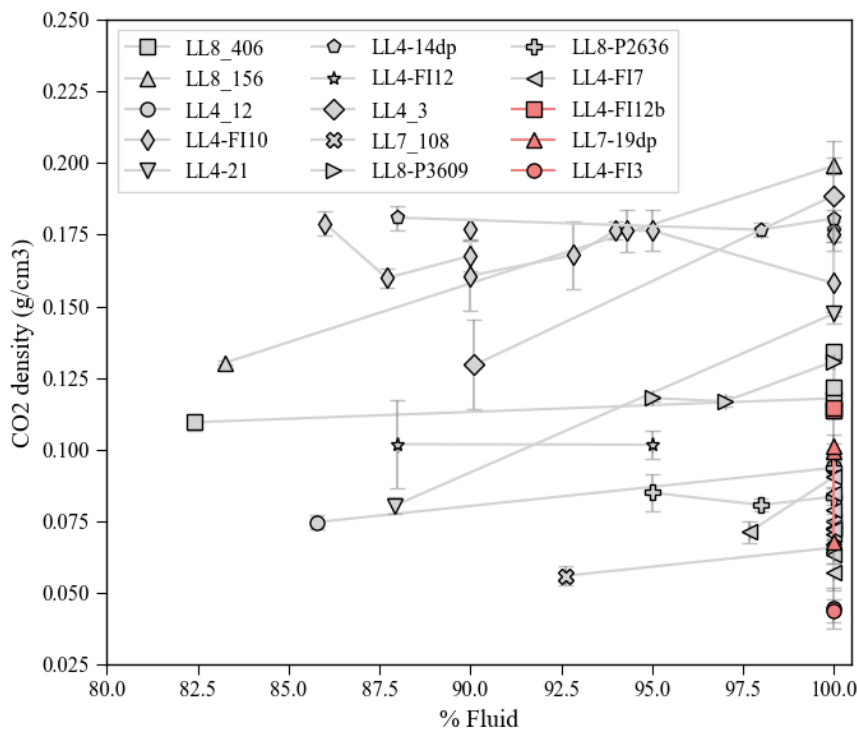

Figure S-12: Measured CO_2 density of FI against the % exsolved fluid for FI "pairs" – these are FI found in the same crystals and relative proximity to each other with apparently similar genetic relationships.

Figure S-13: Single crystal plots (Pages 12-18). Measured CO_2 density of FI against the % exsolved fluid for FI "pairs" – these are FI found in the same crystals and relative proximity to each other with apparently similar genetic relationships.
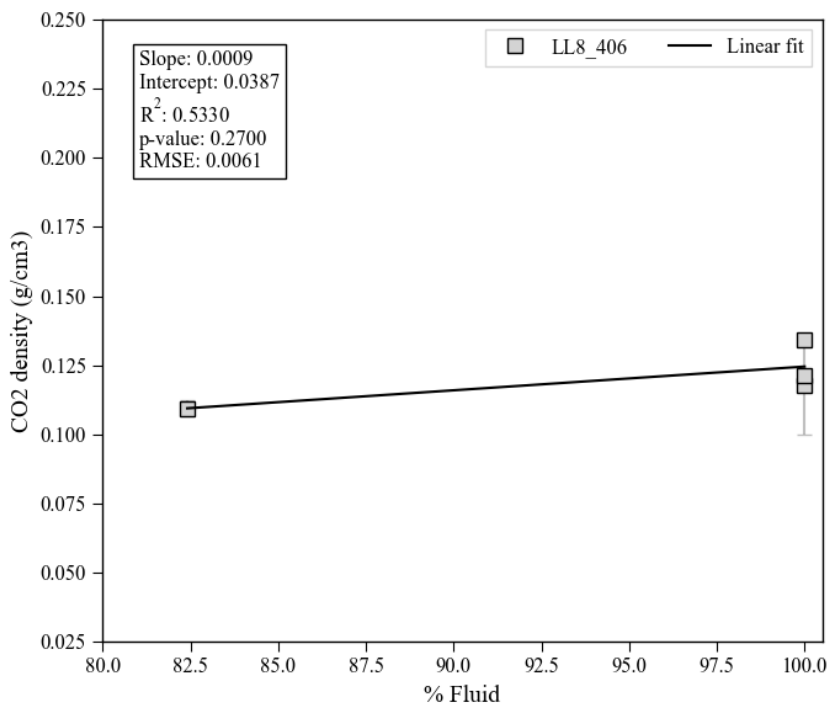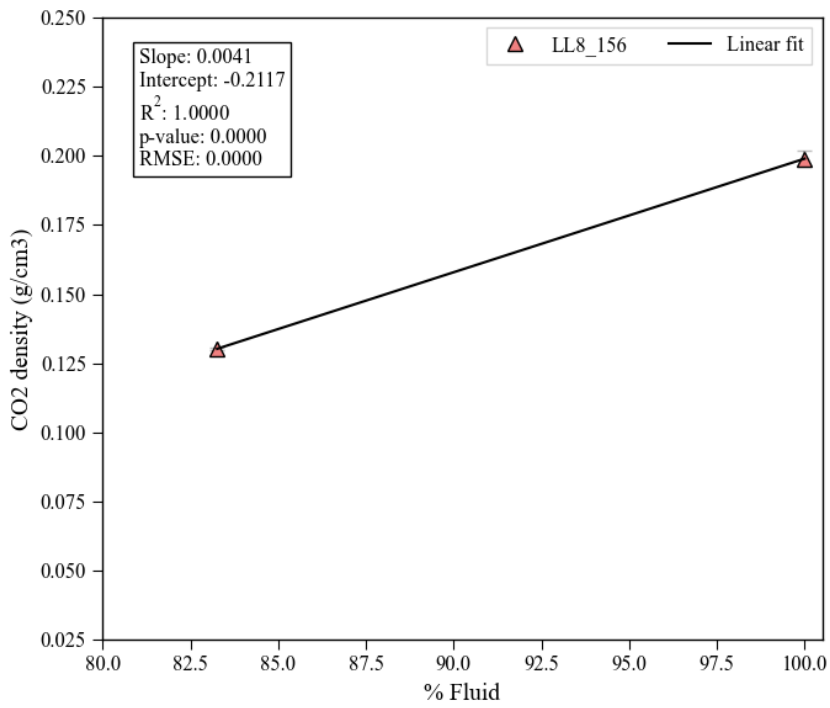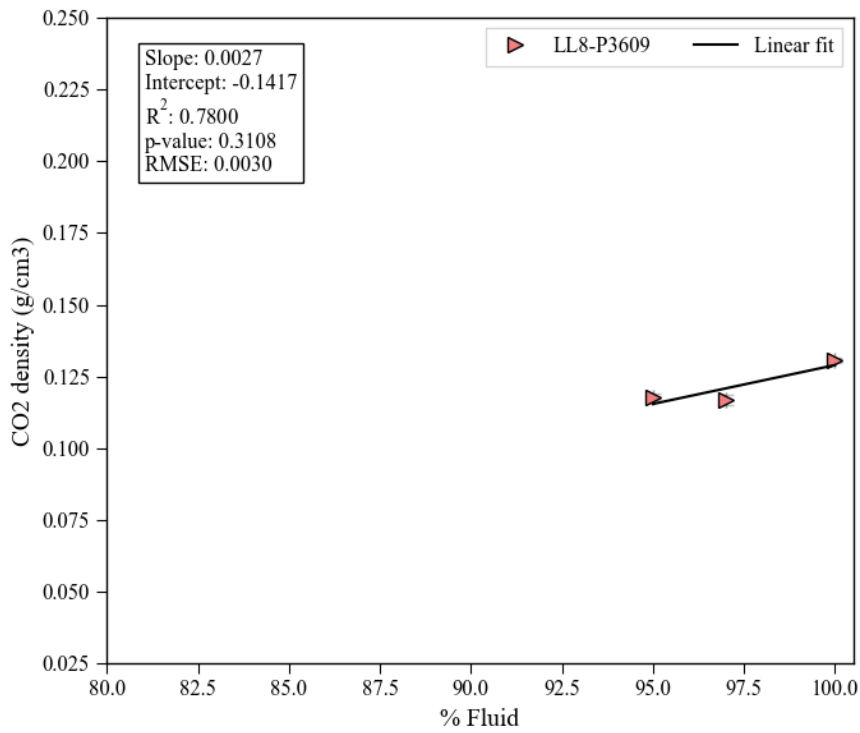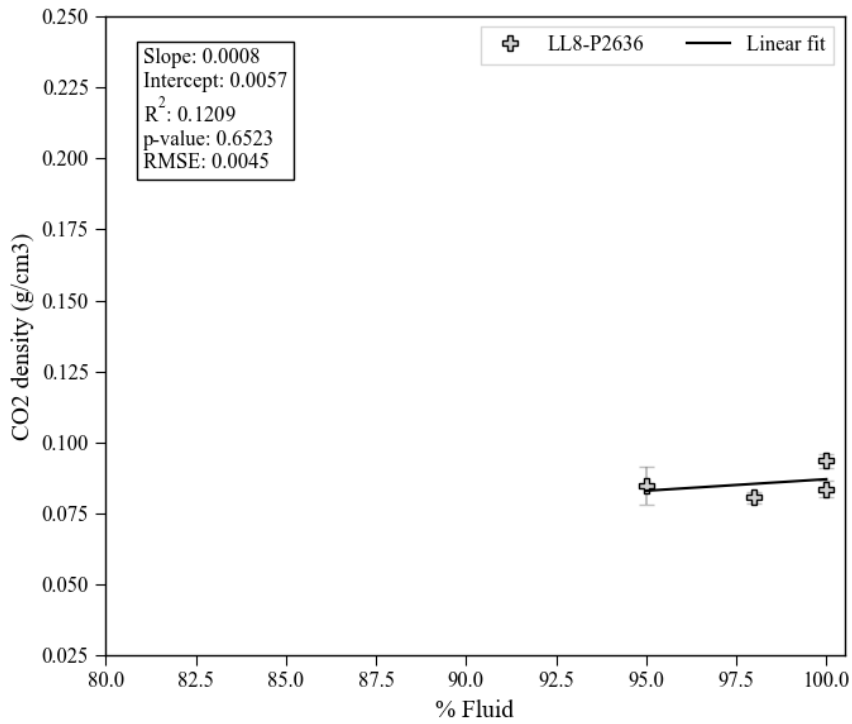
19

22
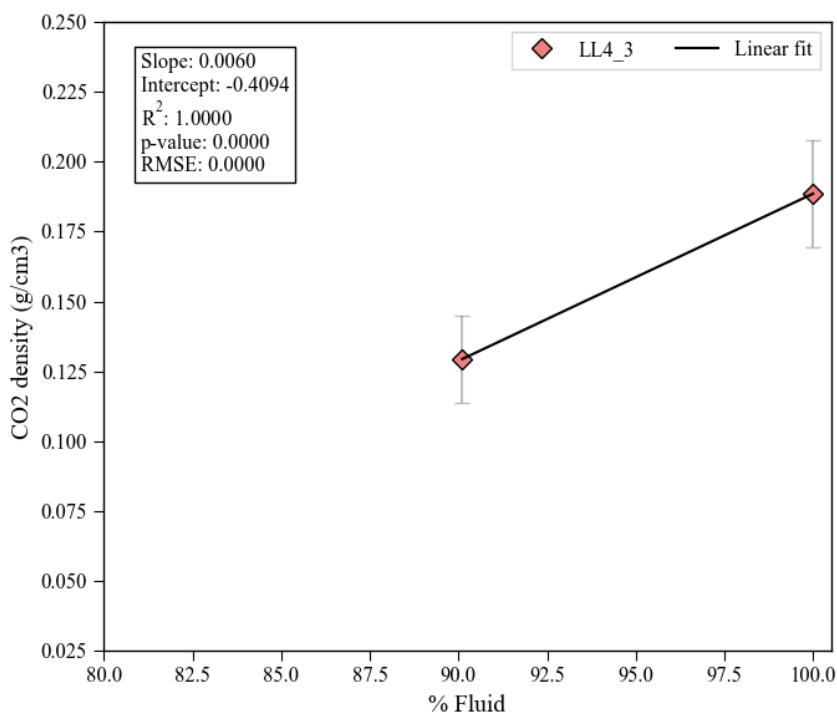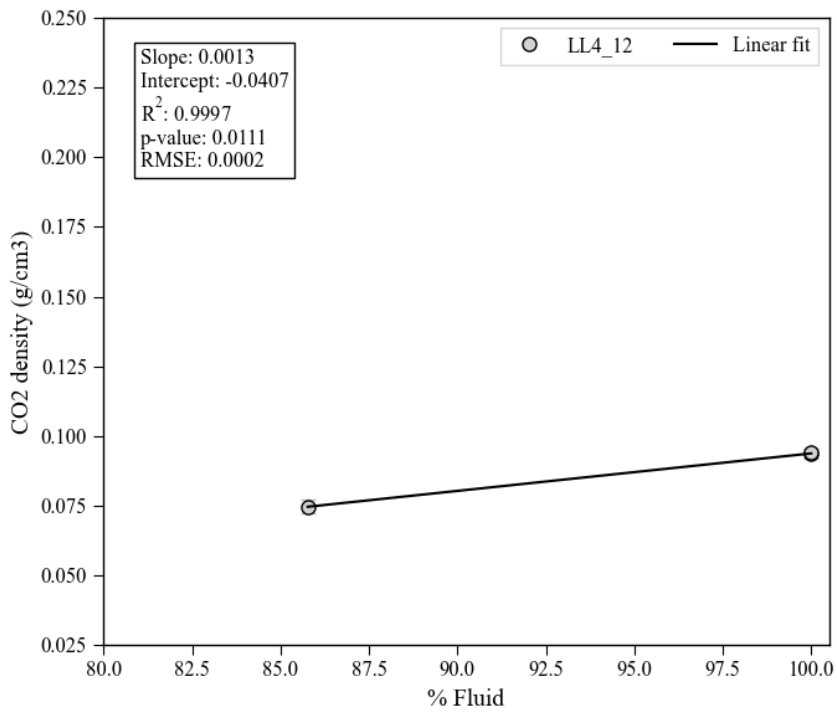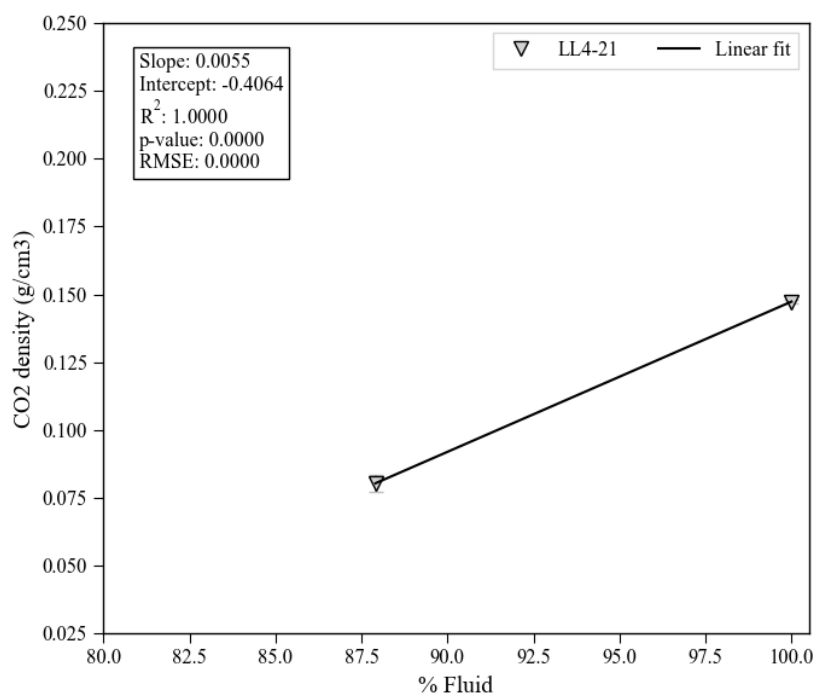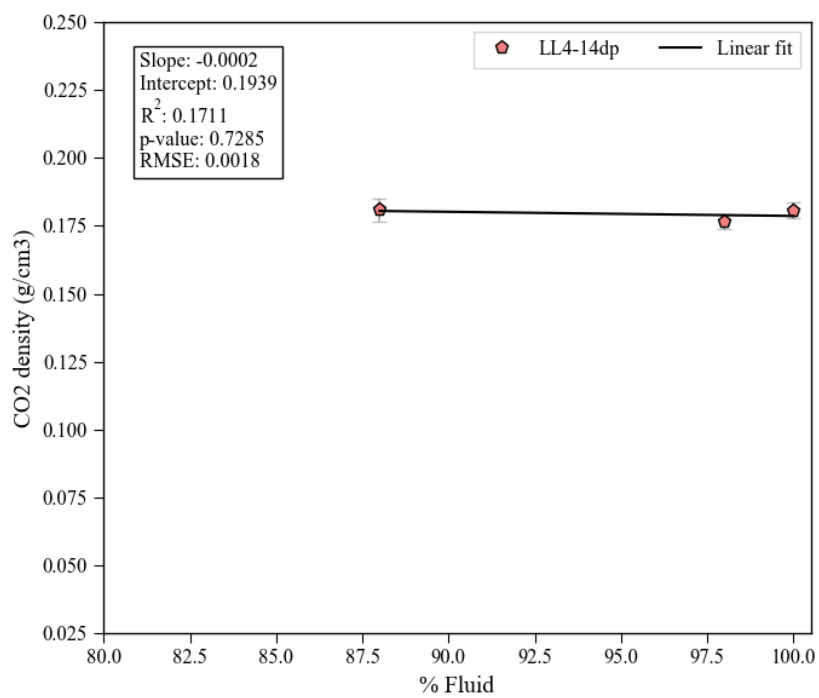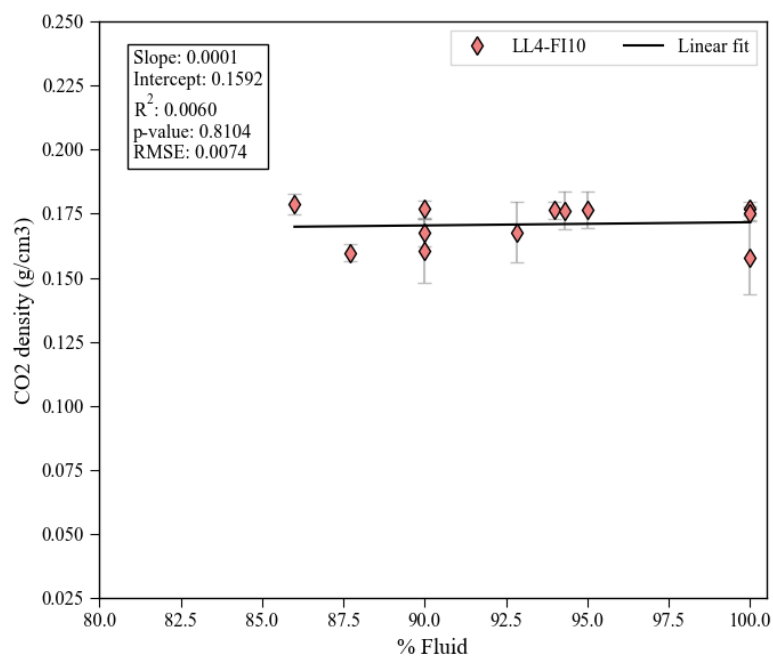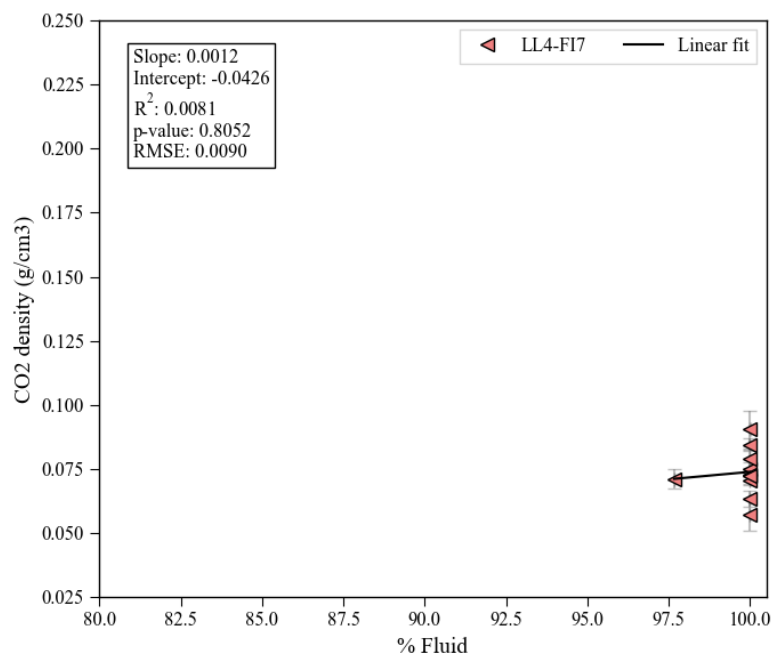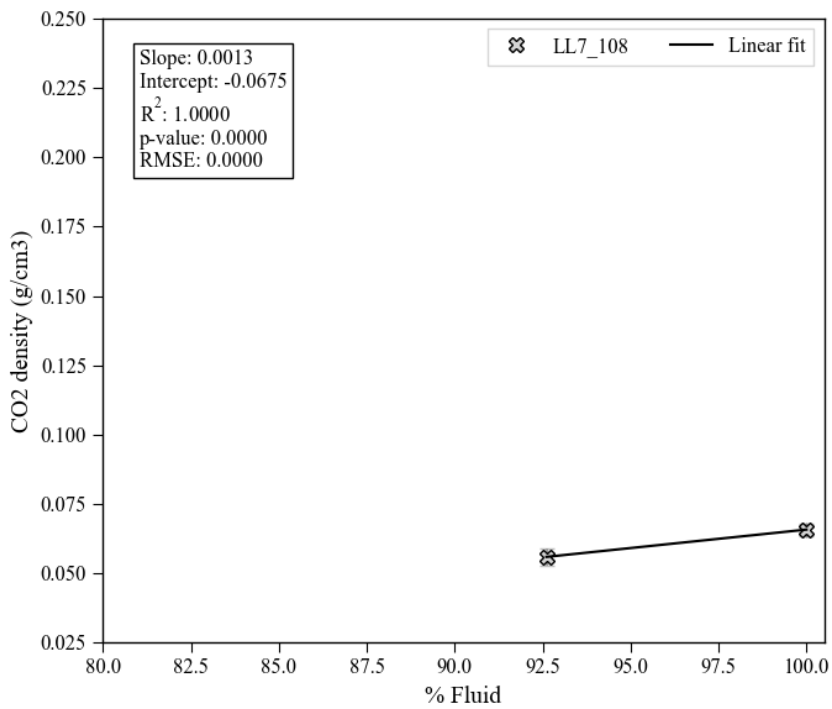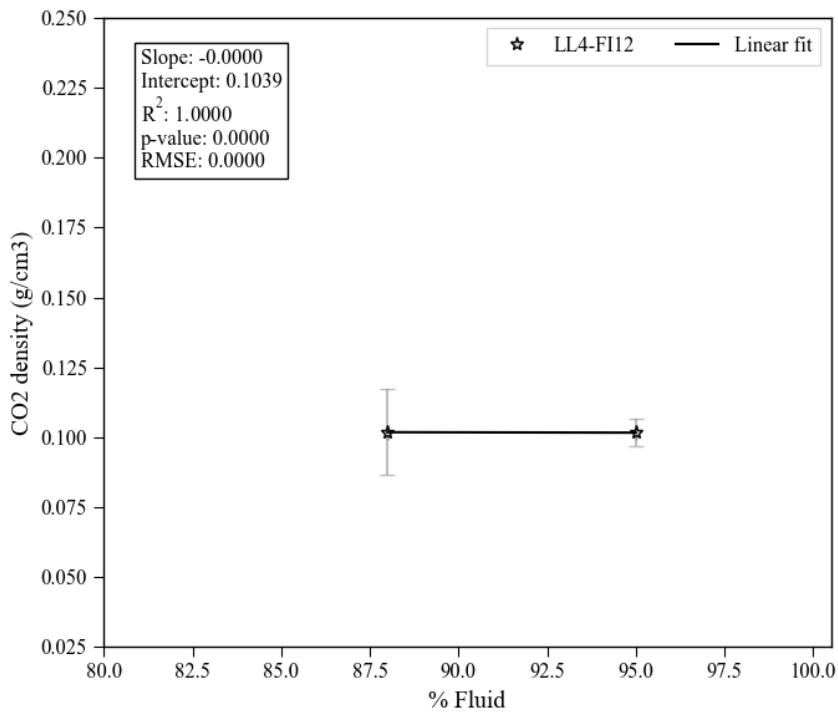
Supplementary information references

Allison, C. M., Roggensack, K. & Clarke, A. B. (2022). MafiCH: a general model for H2O–CO2 solubility in mafic magmas. *Contributions to Mineralogy and Petrology* **177**, 40.

Burke, E. A. J. (2001). Raman microspectrometry of fluid inclusions. *Lithos* **55**, 139–158.

Clague, D. A. & Bohrson, W. A. (1991). Origin of xenoliths in the trachyte at Puu Waawaa, Hualalai Volcano, Hawaii. *Contributions to Mineralogy and Petrology*. Springer **108**, 439–452.

Clague, D. A., Moore, J. G., DIXON, J. E. & Friesen, W. B. (1995). Petrology of submarine lavas from Kilauea's Puna Ridge, Hawaii. *Journal of Petrology*. Oxford University Press **36**, 299–349.

Dayton, K. *et al.* (2023). Deep magma storage during the 2021 La Palma eruption. *Science Advances*. American Association for the Advancement of Science **9**, eade7641.

DeVitre, C. L. *et al.* (2023). Oceanic intraplate explosive eruptions fed directly from the mantle. *Proceedings of the National Academy of Sciences*. Proceedings of the National Academy of Sciences **120**, e2302093120.

DeVitre, C. L., Allison, C. M. & Gazel, E. (2021). A high-precision CO2 densimeter for Raman spectroscopy using a Fluid Density Calibration Apparatus. *Chemical Geology* **584**, 120522.

Ghiorso, M. S. & Gualda, G. A. R. (2015). An H2O–CO2 mixed fluid saturation model compatible with rhyolite-MELTS. *Contributions to Mineralogy and Petrology* **169**, 53.

Hansteen, T. H. & Klügel, A. (2008). Fluid Inclusion Thermobarometry as a Tracer for Magmatic Processes. *Reviews in Mineralogy and Geochemistry* **69**, 143–177.

Helz, R. T., Clague, D. A., Mastin, L. G. & Rose, T. R. (2015). Evidence for large compositional ranges in coeval melts erupted from Kīlauea's summit reservoir. *Hawaiian volcanoes: from source to surface*. Wiley Online Library 125–145.

Helz, R. T., Clague, D. A., Sisson, T. W. & Thornber, C. R. (2014). *Petrologic insights into basaltic volcanism at historically active Hawaiian volcanoes*. *Characteristics of Hawaiian volcanoes*. US Geological Survey, Professional Papers, 237–294.

Helz, R. T., Cottrell, E., Brounce, M. N. & Kelley, K. A. (2017). Olivine-melt relationships and syneruptive redox variations in the 1959 eruption of Kīlauea Volcano as revealed by XANES. *Journal of Volcanology and Geothermal Research*. Elsevier **333**, 1–14.

Iacono-Marziano, G., Morizet, Y., Le Trong, E. & Gaillard, F. (2012). New experimental data and semi-empirical parameterization of H2O–CO2 solubility in mafic melts. *Geochimica et Cosmochimica Acta*. Elsevier **97**, 1–23.

Jarosewich, E., Nelen, J. A. & Norberg, J. A. (1980). Reference samples for electron microprobe analysis. *Geostandards Newsletter*. Wiley Online Library **4**, 43–47.

Lamadrid, H. M., Moore, L. R., Moncada, D., Rimstidt, J. D., Burruss, R. C. & Bodnar, R. J. (2017). Reassessment of the Raman CO2 densimeter. *Chemical Geology* **450**, 210–222.

Lerner, A. H. *et al.* (2021). The petrologic and degassing behavior of sulfur and other magmatic volatiles from the 2018 eruption of Kīlauea, Hawai'i: melt concentrations, magma storage depths, and magma recycling. *Bulletin of Volcanology*. Springer **83**, 1–32.

Lin, F., Bodnar, R. J. & Becker, S. P. (2007). Experimental determination of the Raman CH4 symmetric stretching (v1) band position from 1–650bar and 0.3–22°C: Application to fluid inclusion studies. *Geochimica et Cosmochimica Acta* **71**, 3746–3756.

Moussallam, Y., Edmonds, M., Scaillet, B., Peters, N., Gennaro, E., Sides, I. & Oppenheimer, C. (2016). The impact of degassing on the oxidation state of basaltic magmas: a case study of Kīlauea volcano. *Earth and Planetary Science Letters*. Elsevier **450**, 317–325.

Newman, S. & Lowenstern, J. B. (2002). VolatileCalc: a silicate melt–H2O–CO2 solution model written in Visual Basic for excel. *Computers & Geosciences* **28**, 597–604.

Ryan, M. P. (1987). The elasticity and contractancy of Hawaiian olivine tholeiite, and its role in the stability and structural evolution of sub-caldera magma reservoirs and rift systems. In Volcanism in Hawaii. *US Geol. Surv. Prof. Pap.* **1350**, 1395–1447.

Schindelin, J. *et al.* (2012). Fiji: an open-source platform for biological-image analysis. *Nature Methods* **9**, 676–682.

Shea, T., K. Matzen, A. & J. Mourey, A. (2022). Experimental study of Fe–Mg partitioning and zoning during rapid growth of olivine in Hawaiian tholeiites. *Contributions to Mineralogy and Petrology*. Springer **177**, 114.

Shishkina, T. A., Botcharnikov, R. E., Holtz, F., Almeev, R. R., Jazwa, A. M. & Jakubiak, A. A. (2014). Compositional and pressure effects on the solubility of H2O and CO2 in mafic melts. *Chemical Geology* **388**, 112–129.

Sides, I., Edmonds, M., Maclennan, J., Houghton, B. F., Swanson, D. A. & Steele-MacInnis, M. J. (2014a). Magma mixing and high fountaining during the 1959 Kīlauea Iki eruption, Hawai'i. *Earth and Planetary Science Letters*. Elsevier **400**, 102–112.

Sides, I. R., Edmonds, M., Maclennan, J., Swanson, D. A. & Houghton, B. F. (2014b). Eruption style at Kīlauea Volcano in Hawai'i linked to primary melt composition. *Nature Geoscience*. Nature Publishing Group **7**, 464–469.

Span, R. & Wagner, W. (1996). A new equation of state for carbon dioxide covering the fluid region from the triple-point temperature to 1100 K at pressures up to 800 MPa. *Journal of physical and chemical reference data*. American Institute of Physics for the National Institute of Standards and … **25**, 1509–1596.

Steele-MacInnis, M., Esposito, R., Moore, L. R. & Hartley, M. E. (2017). Heterogeneously entrapped, vapor-rich melt inclusions record pre-eruptive magmatic volatile contents. *Contributions to Mineralogy and Petrology*. Heidelberg, Netherlands: Springer Nature B.V. **172**, 1–13.

Wang, X., Chou, I.-M., Hu, W., Burruss, R. C., Sun, Q. & Song, Y. (2011). Raman spectroscopic measurements of CO2 density: Experimental calibration with high-pressure optical cell (HPOC) and fused silica capillary capsule (FSCC) with application to fluid inclusion observations. *Geochimica et Cosmochimica Acta* **75**, 4080–4093.

Wieser, P. E. *et al.* (2021). Reconstructing Magma Storage Depths for the 2018 Kīlauean Eruption From Melt Inclusion CO2 Contents: The Importance of Vapor Bubbles. *Geochemistry, Geophysics, Geosystems* **22**, e2020GC009364.

Wieser, P. E. & DeVitre, C. L. (2023). DiadFit: An Open-SourcePython3 Tool for Peak fitting of Raman Data from silicate melts and CO2 fluids. EarthArXiv.

Wieser, P. E., Edmonds, M., Maclennan, J., Jenner, F. E. & Kunz, B. E. (2019). Crystal scavenging from mush piles recorded by melt inclusions. *Nature Communications*. Nature Publishing Group **10**, 5797.

Yuan, X. & Mayanovic, R. A. (2017). An Empirical Study on Raman Peak Fitting and Its Application to Raman Quantitative Research. *Applied Spectroscopy*. Society for Applied Spectroscopy **71**, 2325–2338.

Insert your image here

Figure S-1   **(a)** Insert the figure caption here. **(b)**…

Supplementary Information References

Please insert <u>all</u> references cited in the Supplementary Information (including those in any tables and figures) in the list below and then delete these instructions and the examples in the list. Please ensure that the reference list is formatted according to the guidelines given in the Information for Authors, available at: https://www.geochemicalperspectivesletters.org/information-for-authors#References.

Jones, G.U., Smith, L.B. (1995) The Chemistry of Hydrogen. In: James, B.S., Berlin, R.N. (Eds.) *The Elements from A to Z.* Smith-Publishing Inc., New York, 21–34.

Nance, J.R., Armstrong, J.T, Cody, G.D., Fogel, M.L., Hazen, R.M. (2015) Preserved macroscopic polymeric sheets of shell-binding protein in the Middle Miocene (8 to 18 Ma) gastropod *Ecphora*. *Geochemical Perspectives Letters* 1, 1-9.

Strunk Jr., W., White, E.B. (1979) *The Elements of Style*. Third Edition, Macmillan, New York.